nature

https://doi.org/10.1038/s41586-022-04661-w

Accelerated Article Preview

A TMPRSS2 inhibitor acts as a pan-SARS-CoV-2 prophylactic and therapeutic

Received: 14 May 2021

Accepted: 18 March 2022

Accelerated Article Preview
Published online: 28 March 2022

Cite this article as: Shapira, T. et al. A TMPRSS2 inhibitor acts as a pan-SARS-CoV-2 prophylactic and therapeutic. *Nature* https://doi.org/10.1038/s41586-022-04661-w (2022)

Tirosh Shapira, I. Abrrey Monreal, Sébastien P. Dion, David W. Buchholz, Brian Imbiakha, Andrea D. Olmstead, Mason Jager, Antoine Désilets, Guang Gao, Mathias Martins, Thierry Vandal, Connor A. H. Thompson, Aaleigha Chin, William D. Rees, Theodore Steiner, Ivan Robert Nabi, Eric Marsault, Julie Sahler, Diego G. Diel, Gerlinde R. Van de Walle, Avery August, Gary R. Whittaker, Pierre-Luc Boudreault, Richard Leduc, Hector C. Aguilar & François Jean

Article

A TMPRSS2 inhibitor acts as a pan-SARS-CoV-2 prophylactic and therapeutic

https://doi.org/10.1038/s41586-022-04661-w

Received: 14 May 2021

Accepted: 18 March 2022

Published online: 28 March 2022

Tirosh Shapira[1,7], I. Abrrey Monreal[2,7], Sébastien P. Dion[3], David W. Buchholz[2], Brian Imbiakha[2], Andrea D. Olmstead[1], Mason Jager[2], Antoine Désilets[3], Guang Gao[1,4], Mathias Martins[5], Thierry Vandal[3], Connor A. H. Thompson[1], Aaleigha Chin[1], William D. Rees[6], Theodore Steiner[6], Ivan Robert Nabi[4], Eric Marsault[3], Julie Sahler[2], Diego G. Diel[5], Gerlinde R. Van de Walle[2], Avery August[2], Gary R. Whittaker[2], Pierre-Luc Boudreault[3], Richard Leduc[3]✉, Hector C. Aguilar[2]✉ & François Jean[1]✉

The COVID-19 pandemic caused by the SARS-CoV-2 virus remains a global public health crisis. Although widespread vaccination campaigns are underway, their efficacy is reduced due to emerging variants of concern (VOCs)[1,2]. Development of host-directed therapeutics and prophylactics could limit such resistance and offer urgently needed protection against VOCs[3,4]. Attractive pharmacological targets to impede viral entry include type-II transmembrane serine proteases (TTSPs), such as TMPRSS2, whose essential role in the virus lifecycle is to cleave the viral spike protein to expose the fusion peptide for cell entry[5,6]. Here, we identify and characterize a small-molecule compound, N-0385, which exhibits low nanomolar potency and a selectivity index of >10^6 at inhibiting SARS-CoV-2 infection in human lung cells and in donor-derived colonoids[7]. In Calu-3 cells it inhibits entry of SARS-CoV-2 VOCs, B.1.1.7, B.1.351, P.1 and B.1.617.2. Importantly, in the K18-human ACE2 transgenic mouse model of severe SARS-CoV-2 disease, we found that N-0385 affords a high level of prophylactic and therapeutic benefit following either multiple or even a single administration. This demonstrates that TTSP-mediated proteolytic maturation of spike is critical for SARS-CoV-2 infection in vivo and suggests that N-0385 provides a novel effective early treatment option against COVID-19 and emerging SARS-CoV-2 VOCs.

In December 2019, the first cases of coronavirus disease 2019 (COVID-19) emerged in Wuhan, Hubei Province, China, and were rapidly attributed to the etiology of a novel β-coronavirus, severe acute respiratory syndrome coronavirus 2 (SARS-CoV-2)[8]. As of January 18, 2022, more than 332 million SARS-CoV-2 infections and 5.6 million deaths have been reported[9]. The approval and widespread distribution of several highly effective vaccines, along with other public health measures, has been instrumental in controlling the COVID-19 pandemic; however, novel genetic variants of SARS-CoV-2 are emerging and spreading at an alarming rate[10]. Importantly, vaccine effectiveness may be reduced against a number of these variants, termed *variants of concern* (VOCs), including B.1.1.7, P.1, B.1.351 and B.1.617.2[2,11]. In particular, the recent emergence of a novel, heavily mutated VOC, B.1.1.529[1,12] has underlined that the SARS-CoV-2 pandemic is likely to remain a global health threat for the foreseeable future.

Discovery of novel classes of antiviral compounds including both direct-acting (DAA) and host-directed (HDA) antivirals plus intensive *in cellulo* and *in vivo* studies of their antiviral profiles as mono- or combination therapies against emerging SARS-CoV-2 VOCs are critical for developing preventive and therapeutic strategies to combat COVID-19[13,14]. Currently, three antivirals have been approved for clinical use against SARS-CoV-2. Remdesivir is a DAA targeting the viral RNA-dependent RNA polymerase that catalyzes the synthesis of viral RNA[15]. Remdesivir is administered intravenously to hospitalized patients with COVID-19[16]. Other DAAs, PF-07321332 (paxlovid) and MK-4482/EIDD-2801 (molnupiravir), have also been developed as oral clinical candidates[17,18]. Paxlovid targets the coronavirus's main protease ($3CL^{pro}$, also called M^{pro}), an essential protease involved in processing viral replicase polyproteins while molnupiravir is a ribonucleoside analog that inhibits viral replication[17,18]. Alternatively, host-directed

[1]Department of Microbiology and Immunology, Life Sciences Institute, University of British Columbia, Vancouver, BC, Canada. [2]Department of Microbiology and Immunology, Cornell University College of Veterinary Medicine, Ithaca, NY, USA. [3]Department of Pharmacology-Physiology, Faculty of Medicine and Health Sciences, Institut de Pharmacologie de Sherbrooke, Université de Sherbrooke, Sherbrooke, Québec, Canada. [4]Department of Cellular and Physiological Sciences, Life Sciences Institute, University of British Columbia, Vancouver, BC, Canada. [5]Department of Population Medicine and Diagnostic Sciences, Cornell University College of Veterinary Medicine, Ithaca, NY, USA. [6]Department of Medicine, BC Children's Hospital Research Institute, University of British Columbia, Vancouver, BC, Canada. [7]These authors contributed equally: Tirosh Shapira, I. Abrrey Monrea. ✉e-mail: richard.leduc@usherbrooke.ca; ha363@cornell.edu; fjean@mail.ubc.ca

antivirals (HDAs) (also called *indirect-acting antivirals*) are under investigation and may offer a complement to DAAs. HDAs have a reduced potential for resistance by emerging SARS-CoV-2 VOCs since unlike viral genes, host genes possess a low propensity to mutate[5,13]. Camostat mesylate (Cm), for example, has been repositioned as a clinical candidate for treating COVID-19[19]. Cm is a broad-spectrum serine protease inhibitor used to treat pancreatitis that has demonstrated activity against numerous serine proteases[4,5].

To date, accumulating evidence has demonstrated SARS-CoV-2 dependence on host pathways including the hijacking of TMPRSS2-related proteases for viral entry, suggesting that TTSPs are attractive therapeutic targets to prevent SARS-CoV-2 infection[5,6,20]. The SARS-CoV-2 lifecycle begins with attachment and entry into respiratory epithelium via the angiotensin-converting enzyme 2 (ACE2) receptor[4,8]. This is mediated by the major viral surface glycoprotein, spike (S), which must undergo two sequential proteolytic cleavages by host proteases before it can mediate fusion of the virus with host cell membranes, a requirement for subsequent viral replication[3,21,22]. The first spike cleavage occurs at the S1/S2 site, releasing S1 and S2 subunits that remain non-covalently linked, an event likely mediated by host furin-like proteases[21,22]. The second cleavage occurs at the S2' site, immediately adjacent to the fusion peptide. This cleavage, which triggers the fusion event, is mediated by host TTSPs, such as TMPRSS2 and TMPRSS13, which cleave after specific single arginine or lysine residues (Arg/Lys↓)[4,23].

The K18-hACE2 mouse model (transgenic expression of human ACE2 under a cytokeratin 18 promoter) offers a stringent system for testing the efficacy of DAAs and HDAs against severe disease and mortality following SARS-CoV-2 infection[24]. To date, only a few studies have tested antiviral efficacy in this animal model with only one DAA reported as protective against lethal SARS-CoV-2 infection in this model[25,26].

Here, we report on the design and testing of novel peptidomimetics for their inhibitory activity against TMPRSS2 and related TTSPs. We then investigated the peptidomimetics' antiviral activities against SARS-CoV-2 and four variants B.1.1.7 (Alpha), B.1.351 (Beta), P.1 (Gamma), and B.1.617.2 (Delta) in human lung cells. Lastly, we tested our lead highly potent antiviral, N-0385, against SARS-CoV-2 (lineage A strain) and SARS-CoV-2 Delta VOC-induced morbidity and mortality in K18-hACE2 mice. We found that N-0385 affords a high level of protection and a therapeutic benefit following either multiple or even a single administration in this model of severe disease. Thus, N-0385 is a novel antiviral with high potential for use against COVID-19.

Peptidomimetics potently inhibit TMPRSS2

We previously designed first-generation peptidomimetic tetrapeptide compounds with ketobenzothiazole warheads, and they demonstrated inhibitory activity against a host TTSP, matriptase[27,28]. These compounds act as slow tight-binding inhibitors *in vitro* but their potency in cellular systems was modest against influenza A virus[28]. To improve their stability and potency, we modified their N-terminus either by capping or through synthesis of desamino moieties (Fig. 1A and Extended Data Fig. 1A)[29]. When we measured the stability of the desamino compounds, we found that they had drastically increased half-lives compared to their corresponding amine analogs (48 hr vs. 2 hr, respectively, in human lung epithelial Calu-3 cells) (data not shown). Moreover, these compounds exhibited low nanomolar efficacies when tested in H1N1 models of influenza A virus infection[28,30].

Expanding on that work here, we developed a small library of peptidomimetic compounds (Fig. 1A and Extended Data Fig. 1A) to screen for inhibition of TMPRSS2 proteolytic activity, as this TTSP is a crucial host protease involved in cleaving the SARS-CoV-2 spike and priming the virus for cell entry[4]. We included in this screen our first-generation tetrapeptide, N-0100[28], which lacks an N-terminal stabilizing group, along with three desamino tetrapeptide analogs. We also tested four tripeptides containing different N-terminal capping groups.

To evaluate the efficacies of these compounds, we set up a cellular assay to measure TMPRSS2-dependant pericellular inhibition of proteolytic activity. We expressed the full-length, wild type TMPRSS2 or an inactive form of the protease in which the serine residue of the catalytic triad was replaced by alanine (TMPRSS2-S441A) in Vero E6 cells. Twenty-four hr after transfection, the media was replaced for an additional 24 hr with serum-free media containing vehicle or compound in the presence of a TMPRSS2-preferred fluorogenic substrate[31] (Fig. 1B). Using this assay, we show that, as expected, the S441A substitution completely abrogated TMPRSS2 proteolytic activity.

The peptidomimetics were initially tested for inhibitory activity against human TMPRSS2 at 10 nM (Fig. 1B). Camostat mesylate (Cm), which has previously been shown to be active against TMPRSS2[23], reduced substrate proteolysis by 56% compared to untreated TMPRSS2-expressing cells. The first-generation peptidomimetic, N-0100, did not inhibit TMPRSS2 activity under these conditions. However, the more stable tetrapeptides with N-terminus desamino moieties, N-0130 and N-0438, had increased inhibitory activity of 72% and 84%, respectively. N-0678 (substituting P2 Phe for the synthetic amino acid cyclohexylalanine (Cha)) only inhibited TMPRSS2 activity by 5%. N-0676 (a tripeptide with an N-terminal Ac cap and P2 Cha) also weakly inhibited TMPRSS2 activity by 8%. N-0386 (with restored Phe in P2) resulted in a more potent inhibition of 73%. N-1296 (replacing Ac with Am) had reduced potency of 16%, while N-0385 (replacing Am with Ms) resulted in a highly potent inhibition of 83%. Importantly, several peptidomimetic compounds were more efficient than Cm at reducing TMPRSS2 activity (Fig. 1B).

We then investigated the dose response of the four most promising peptidomimetics (N-0130, N-0385, N-0386, and N-0438). The half-maximal inhibitory concentration (IC_{50}) of Cm was 17.5 ± 18.8 nM, while the IC_{50} for N-0130 was 3.1 ± 1.5 nM; for N-0438 it was 5.2 ± 5.4 nM; for N-0386 it was 3.9 ± 4.4 nM; and for N-0385 it was 1.9 ± 1.4 nM (Fig. 1C and Extended Data Table 1). Importantly, none of the compounds affected Vero E6 cellular viability when used at 10 μM (Extended Data Fig. 1B). To confirm the contribution of the ketobenzothiazole warhead to the molecule's inhibitory activity, the ketone functional group of N-0385 was replaced with an alcohol group to generate N-0385(OH) (Fig. 1A), which we expected would no longer trap the target protease. As expected, no significant reduction in TMPRSS2 activity was detected when cells were treated with up to 10 μM of N-0385(OH) (Fig. 1C), suggesting that the integrity of the ketobenzothiazole group is required to achieve potency. We also confirmed the efficacy of N-0385 against murine TMPRSS2 with an IC_{50} of 12.3 ± 1.9 nM (Extended Data Fig. 1C). Next, we sought to determine the selectivity profile of these inhibitors by measuring the dissociation constant K_i on selected recombinant serine proteases, including three members of the TTSP family (matriptase, hepsin, DESC1) as well as furin, thrombin, and cathepsin L. All four peptidomimetic compounds we tested behaved as low nanomolar inhibitors for the TTSPs, but they were inactive or showed only weak inhibition against the other proteases (Fig. 1D and Extended Data Table 2). Cm displayed a similar selectivity profile to the peptidomimetics tested, except that it demonstrated moderate inhibition of thrombin (K_i = 621 nM) in line with its broader spectrum properties. Overall, TTSP-targeting peptidomimetics harbouring a ketobenzothiazole warhead inhibit TMPRSS2-dependent pericellular activity in a cellular assay and preferentially inhibit other members of the TTSP family.

To understand the mode of binding and the main interactions of our inhibitors and how these compounds achieve their high inhibitory potential, we built a homology model of TMPRSS2 using the crystal structure of matriptase (PDB: 6N4T)[32]. Alignment of the catalytic domains demonstrated 41% and 60% identity and sequence similarity, respectively, making it a reliable model, especially near the conserved binding site. Docking of N-0385 was modeled to this structure (Fig. 1E). As predicted and recently published[32], the catalytic triad

Ser441 (catalytic triad: Ser441, His296, and Asp345; Fig. 1E inlet) forms a covalent bond with the warhead ketone, thus leading to a tight-binding mode of inhibition.

Several key interactions can be observed in the binding pocket. As in all TTSP inhibitors possessing a guanidine group on the sidechain, a strong hydrogen bond network stabilizes this pharmacophore deep within the binding pocket (Fig. 1E). This includes Asp435 and Gly464 as well as Gln438 via a water molecule. Gln438 is also involved in another hydrogen bond of this same water molecule to the oxygen of the main-chain ketone group. This ketone also acts as a hydrogen bond acceptor with Gly462. The N-terminal mesylate forms two hydrogen bonds, one intramolecular with the side-chain amide of the Gln residue of N-0385 and another with Gly462. Finally, the oxygen of the newly formed hemiacetal is stabilized by two hydrogen bond donors from the Gly439 and Ser441 amines. A portion of the ketobenzothiazole warhead and the aromatic ring from the phenylalanine are exposed to the solvents, which could allow us to further optimize the design of this second-generation inhibitor leading to an improved pharmacokinetic profile.

N-0385 inhibits SARS-CoV-2 infection

The peptidomimetic compounds we screened against TMPRSS2 were subsequently tested for their efficacy at preventing SARS-CoV-2 infection. Calu-3 cells were pretreated with 100 nM of the compounds for three hr prior to infection with an original SARS-CoV-2 lineage B strain (VIDO). Cells were fixed and immunofluorescently stained for dsRNA, a marker of viral replication[33], and for the viral nucleocapsid, a marker of viral entry and translation[6] (Extended Data Fig. 2). Fluorescent high-content imaging and relative quantification of virally infected cells demonstrated consistent inhibitory profiles across dsRNA and nucleocapsid staining, which mirrored the inhibitory profile observed in the TMPRSS2 proteolytic activity assay (Fig. 2A vs. Fig. 1B). Cm, which interferes with SARS-CoV-2 infection[4], reduced infection by >83% compared to non-treated cells. N-0100, which lacks an N-terminal stabilizing moiety, reduced infection by <25%. The tetrapeptides N-0130 and N-0438, which have N-terminus desamino moieties, had greatly increased antiviral activity of >93% and >88%, respectively. N-0678 (substituting P2 Phe for the synthetic amino acid Cha) inhibited SARS-CoV-2 by <23%. N-0676 (tripeptide with an N-terminal Ac cap and P2 Cha) had only moderate inhibitory activity of <53%. N-0386 (with restored Phe in P2) resulted in a highly potent SARS-CoV-2 inhibition of >99%. N-1296 (replacing Ac with Am) reduced the antiviral potency to <44%, while N-0385 (capped with Ms) restored antiviral activity to >99%. Last, N-0385(OH) (with OH replacing the functional group of the warhead), demonstrated a <23% inhibition of SARS-CoV-2. Thus, TMPRSS2-inhibiting peptidomimetics are also inhibitors of SARS-CoV-2 replication and translation in Calu-3 cells; the stabilizing N-terminal caps and the ketobenzothiazole warhead are likely essential for compound stability and antiviral potency.

Compounds significantly inhibiting SARS-CoV-2 (>75%) in the antiviral screen were further validated and characterized using a dose response analysis in Calu-3 cells (Fig. 3). The half-maximal effective concentration (EC_{50}) of Cm was 10.6 ± 8.4 nM, while the EC_{50} for N-0130 was 30.1 ± 30.1 nM; for N-0438 it was 35.7 ± 24.5 nM; for N-0386 it was 2.3 ± 1.7 nM; and for N-0385 it was 2.8 ± 1.4 nM (Fig. 2B). An EC_{50} value could not be determined for N-0385(OH) as significant inhibition was not observed at concentrations up to 1 μM (Fig. 2B, Extended Data Fig. 2). These compounds did not exhibit any toxicity; all four compounds had half-maximal cytotoxic concentration (CC_{50}) values of >1 mM in Calu-3 cells (Table S1, Extended Data Fig. 3). Thus, the selectivity index (SI) for these compounds (N-0130, N-0438, N-0386, and N-0385) was between 8.97×10^4 and 2.75×10^6 (Extended Data Table 1). Overall, these results confirm that two newly discovered TTSP-targeted peptidomimetic compounds (N-0386 and N-0385) are extremely potent low nanomolar inhibitors of SARS-CoV-2 infection in human lung epithelial cells.

We next examined the impact of Cm, N-0385, and N-0385(OH) on the extracellular release of SARS-CoV-2 infectious virions from Calu-3 cells. Two effective doses (40 nM and 200 nM) from the EC_{50} curve-fitting (Fig. 2B) were selected for plaque assays. The cell supernatant from Cm-treated and Cm-infected cells demonstrated ~ half-log reduction in the presence of 40 nM compared to the DMSO-treated and infected control and a ~1.5-log reduction with 200 nM Cm (Fig. 2C). In comparison, both 40 nM and 200 nM treatments with N-0385 reduced viral titers by almost 2-log. Consistent with previous results, N-0385(OH) did not exhibit a significant reduction in SARS-CoV-2 plaques at 40 nM or 200 nM. These results confirm that N-0385, which targets TMPRSS2, is a potent inhibitor of SARS-CoV-2 infectivity in Calu-3 cells and that the ketobenzothiazole warhead is required for N-0385 antiviral potency.

Although Calu-3 cells represent a scalable and clinically relevant system of antiviral screening for SARS-CoV-2 inhibitors, they are an immortalized cell line. To evaluate the effectiveness of N-0385 in a primary human cell-based model, we explored SARS-CoV-2 infection in donor-derived human colonoids[34,35]. SARS-CoV-2 initially causes a respiratory infection but many infected individuals also experience gastrointestinal symptoms frequently linked with increased disease duration and severity[36]. A recent report demonstrated TMPRSS2 as an essential co-factor for SARS-CoV-2 infection in colonoids[20]. We first relatively quantified mRNA expression of ACE2 and TMPRSS2 in colonoids and Calu-3 cells using qPCR. ACE2 demonstrated comparable expression in colonoids compared to Calu-3 cells, while TMPRSS2 demonstrated much higher expression in colonoids compared to Calu-3 cells (Extended Data Fig. 1D, E). We then investigated the susceptibility of colonoid monolayers to SARS-CoV-2 infection. Consistent with previous work, the colonoids were susceptible to infection as evidenced by dsRNA and nucleocapsid staining (Fig. 2D and Extended Data Fig. 4).

N-0385 and N-0385(OH) were then tested for their efficacy at preventing SARS-CoV-2 infection in colonoids. The colonoids were pretreated with 100 nM of the compounds for 3 h prior to 3-day infection with SARS-CoV-2. Under these conditions, N-0385-pretreated colonoids had undetectable infection compared to DMSO-treated colonoids (>99% inhibition) (Fig. 2D). In contrast, N-0385(OH) did not significantly reduce SARS-CoV-2 infection in this system (<20% inhibition) (Fig. 2D). These results align with observations in Calu-3 cells and confirm the nanomolar potency of N-0385 against SARS-CoV-2 in primary human cells.

N-0385 inhibits SARS-CoV-2 VOC infection

To our knowledge, mutations in the TMPRSS2 cleavage site have not been identified in SARS-CoV-2 variants, suggesting that N-0385 should retain high potency against SARS-CoV-2 VOCs[11]. First, we confirmed infectivity of four VOCs in Calu-3 cells: B.1.1.7 (Alpha), B.1.351 (Beta), P.1 (Gamma), and B.1.617.2 (Delta). Confocal imaging of infected cells confirmed infectivity of these variants as demonstrated by nucleocapsid and dsRNA staining (Fig. 3A). While the viral marker staining patterns were relatively consistent in Calu-3 cells infected with a lineage B isolate (VIDO), B.1.1.7, B.1.351, and P.1, we observed a striking spheroid-like phenotype in B.1.617.2-infected cells (Fig. 3A, B, Supplementary Video 1). We then evaluated the efficacy of N-0385 for preventing SARS-CoV-2 VOC infection in Calu-3 cells. The EC_{50} of N-0385 against all VOCs was in the low nanomolar range, ranging from 2.1 nM to 13.9 nM using nucleocapsid staining as a marker, and ranging from 2.6 nM to 26.5 nM using dsRNA staining as a marker of infection (Fig. 3C, D). This underlines the potential of N-0385 to act as a pan-variant, host-directed antiviral against emerging SARS-CoV-2 VOCs.

N-0385 protects mice against COVID-19

After establishing the efficacy of N-0385 *in vitro* and *in cellulo*, we tested whether intranasal administration would improve morbidity and survival *in vivo*, using K18-hACE2 mice expressing the human ACE2 receptor driven by a keratin promoter[37,38], an established mouse model of severe

SARS-CoV-2 disease[39]. Dosing regimens and drug concentrations were chosen based on preliminary studies performed in a mouse model of influenza A virus infection demonstrating antiviral efficacy at 7.2 mg/kg (data not shown), based on the solubility of N-0385 and on knowledge that K18-hACE2 mice typically survive 6 to 8 days post-infection (dpi) with SARS-CoV-2[40]. Ten mice per group (five females and five males) were administered a single daily intranasal dose of 7.2 mg/kg N-0385, N-0385(OH), or a vehicle control (0.9% saline) for eight days from day -1 to day 6 relative to infection. The mice were challenged on day 0 with 1×10^3 PFU/mouse of SARS-CoV-2 and surviving mice were monitored until the study endpoint (14 dpi) (Fig. 4A). At 6 dpi (before any mice had died) the saline control and N-0385(OH) treated mice lost on average 14% and 12% of their weight, respectively, while N-0385 treated mice lost on average only 3% weight. The relative changes in weight were maintained when compared at the study endpoint (14%, 15% and 3% weight loss for saline, N-0385(OH), and N-0385 treated mice, respectively) (Fig. 4B–E). As expected, the majority of saline and N-0385(OH)-treated mice died 6-9 dpi, with 0% and 10% surviving to the endpoint, respectively. In contrast, 70 % of N-0385-treated mice survived to the endpoint (Fig. 4F).

In this first *in vivo* experiment, histological examination of lung tissue obtained either at time of death (6-9 dpi) or study endpoint (14 dpi) revealed mild pathology in most SARS-CoV-2 infected mice, with mild perivascular and interstitial inflammatory infiltrates as the predominant change, irrespective of treatment group (Extended Data Table 3). Compared to N-0385-treated mice, control saline-treated mice frequently had additional histological changes including alveolar edema, alveolar fibrin, and inflammatory cells within alveoli. Of the mice that survived up to the study endpoint, three had focal areas of fibrosis, type II pneumocyte hyperplasia, and occasionally lymphoid hyperplasia. However, most of the mice that survived showed little to no pathological signs in the lungs (Fig. 4G). Histologic lesions in the brain included multifocal perivascular cuffs of inflammatory cells, reactive glial cells, neutrophils, and lymphocytes in the adjacent neuroparenchyma (gliosis), infiltration of the meninges with inflammatory cells, and neuronal necrosis characterized by shrunken neuron bodies with hypereosinophilic cytoplasm and pyknotic or karyorrhectic nuclei. No lesions were observed in the brains of mice that survived to the study endpoint (Fig. 4H and Extended Data Table 3). Immunohistochemistry (IHC) of the SARS-CoV-2 nucleocapsid protein and plaque assay from the tissues harvested at time of death (6-9 dpi) or endpoint (14 dpi) revealed significant amounts of the viral antigen and high viral titers in the tissues of infected mice treated with saline or N-0385(OH). (Extended Data Fig. 5 and Extended Data Table 4). Although samples obtained at different timepoints are not directly comparable, the amount of antigen and viral titers were lower in mice treated with N-0385, particularly in those that survived to the study endpoint (Extended Data Fig. 5).

After establishing that N-0385 improves survival of SARS-CoV-2 infected mice, we evaluated the outcome of a shortened treatment regimen (4 days) on K18-hACE2 mouse survival (Fig. 5). Further, to accurately compare viral loads post-infection, we also analyzed viral lung titers and IHC at the same timepoint (3 dpi) in equivalently infected mice groups, in addition to analyzing titers at the time of death or the study endpoint (14 dpi). Five female and 5 male mice per group were treated with N-0385 or saline from day -1 to day 2 relative to infection (Fig. 5A). The N-0385-treated mice in this group showed 100% survival compared to 20% survival in the control group (Fig. 5B). At 6 dpi (before any mice had died) the saline control mice lost on average 10% of their weight, while N-0385 treated mice gained 1% weight. When compared at time of death or the study endpoint, the saline control mice lost an average 14% weight, while N-0385 treated mice gained 2 % weight (Fig. 5C–E). Our analysis of viral loads via plaque assays and IHC at 3 dpi demonstrated that N-0385 treated mice had significantly reduced viral titers (97%) and IHC staining (98%), compared to control saline-treated mice (Fig. 5F, G). No infectious virus was detected in the lung of N-0385-treated mice at the study endpoint, or in the two saline treated mice that survived to the endpoint. (Fig. 5H). This underlines the effectiveness of N-0385 in blocking SARS-CoV-2 infection and improving disease outcomes and survival using a short, early treatment regimen.

N-0385 protects mice against Delta VOC

Next, we further investigated the treatment window of N-0385 as well as the pan-variant effectiveness against SARS-CoV-2 B.1.617.2 in mice using single doses of N-0385. Mice (5 males and 5 females per group) were challenged on day 0 with 1×10^3 PFU/mouse of SARS-CoV-2 B.1.617.2 (Fig. 6). Mice administered a single intranasal dose of saline 12 hours post-infection (hpi) (Fig. 6A) were compared to mice treated with N-0385 12 hpi (N-0385 12 hpi, 14.4 mg/kg) (Fig. 6B), or at the time of infection (N-0385 0 hpi, 7.2 mg/kg) (Fig. 6C). Weight was monitored for 6 days post-infection. N-0385 demonstrated significant protection against infection-associated weight loss (Fig. 6D); the lowest weight loss occurred when N-0385 treatment was administered at the time of infection (0 hpi) (2% weight gain vs. 13% weight loss in control mice) (Fig. 6C, D). Protection also occurred when mice were treated 12 hpi with N-0385 (5% weight loss vs. 14% weight loss in controls) (Fig. 6B and D). In a similar experiment, mice were treated with N-0385 or saline control at 12 hpi and lung tissue was harvested 3 dpi for plaque assays and IHC to measure viral titers and nucleocapsid staining (Fig. 6E, F). This demonstrated >50% reduction in viral titers and IHC viral staining in N-0385-treated mice compared to the control saline group. Similarly, total pathology scores of lung tissue assessed using IHC sections were improved by approximately 1.9-fold (or 46%) (Fig. 6G, Extended Data Table 5). Taken together, the *in vivo* data strongly indicate that N-0385 significantly prevents morbidity, mortality, and reduces viral burden in the K18-hACE2 mouse model of severe SARS-CoV-2 disease, when used as a prophylactic or therapeutic treatment.

Discussion

In the present study, we report on N-0385, a potent small-molecule protease inhibitors of human TMPRSS2 and the first SARS-CoV-2 pan-variant HDA effective *in vivo* against the Delta B.1.617.2 VOC. N-0385 acts as an inhibitor of the TTSP-dependent proteolytic activation of virus spike protein, a critical step in permitting viral-cell membrane fusion and entry into target cells[4]. The nanomolar potency of N-0385 against SARS-CoV-2 infection in human Calu-3 cells and patient-derived colonoids without detectable toxicity yields a striking selectivity index of $>10^6$. Furthermore, in the K18-hACE2 mouse model, treating with N-0385 resulted in complete protection against SARS-CoV-2 induced mortality and significantly protected against weight loss, lung pathology, and viral infection when treatment occurred at the time of, or 12 hours after, infection with the SARS-CoV-2 B.1.617.2, suggesting that N-0385 may provide a novel effective early treatment option against emerging SARS-CoV-2 VOCs.

We have previously shown how peptidomimetic-based compounds with ketobenzothiazole warheads exhibited potent antiviral efficacy at impeding influenza A H1N1 virus infection of Calu-3 cells through inhibition of TTSPs[28]. The activation of the influenza A virus surface glycoprotein hemagglutinin is strikingly similar to that of the SARS-CoV-2 spike in that both are viral surface protein homotrimers cleaved by proteolytic enzymes of the TTSP family that are expressed by host epithelial cells[14,41]. TTSPs are attractive broad-spectrum, HDA drug targets because of (i) their important role in mediating viral entry[5]; (ii) their accessibility on the surface of nasal and pulmonary epithelial cells[42,43]; and (iii) their demonstrated therapeutic potential for combating medically important viruses such as SARS-CoV-2 and other human coronaviruses as well as influenza viruses[14,41,44].

In this work, we present the design and use of peptidomimetics with ketobenzothiazole warheads, which led to the identification of N-0385,

a compound with potent inhibitory activity against TMPRSS2 proteolytic activity (IC_{50} = 1.9 nM). When we screened selected TMPRSS2 inhibitors for antiviral activity against SARS-CoV-2, a similar inhibitory profile was observed against TMPRSS2 expressed in Vero E6 cells compared to SARS-CoV-2 infection in Calu-3 cells. N-0385, the lead antiviral candidate, demonstrated potent inhibition of SARS-CoV-2 infection in Calu-3 cells, with an EC_{50} of 2.8 ± 1.4 nM and a SI of > 1×10^6. The potency of N-0385 was validated using two viral biomarkers of intracellular infection as well as by measuring the release of infectious viral particles. Further, complete inhibition of infection was achieved with 100 nM N-0385 in colonoids derived from human donors confirming the low nanomolar potency of N-0385 against SARS-CoV-2. This complements a recent report demonstrating that peptidomimetic compounds targeting TMPRSS2 have high potency against SARS-CoV-2-induced cytopathic effect, as well as excellent stability and safety in mice[45].

The usefulness of N-0385 needs to be envisaged in the context of circulating SARS-CoV-2 variants. VOCs such as B.1.1.7, P.1 and B.1.617.2 were of concern because of their rapid rise to dominance as well as their extensive spike mutations, which could lead to conformational changes of the trimeric spike structure, which in turn may be detrimental to antiviral effectiveness and vaccine protection[2,11]. In 2021, B.1.617.2 became the dominant circulating variant for which reduced vaccine efficacy and worse infection outcomes were documented[2]. We hypothesized that N-0385 efficacy against four SARS-CoV-2 VOCs (B.1.1.7, P.1, B.1.351 and B.1.617.2) should not be compromised since no mutations in the TMPRSS2 cleavage site have been reported[2,11]. Our results confirmed low nanomolar pan-variant antiviral activity of N-0385 against these four SARS-CoV-2 VOCs in human cells.

Recent studies have shown that the K18-hACE2 mouse model used in our studies is an ideal model for recapitulating severe human COVID-19 pathology as well as high morbidity and mortality. The SARS-CoV-2 challenge in this model leads to high viral titers in lung and brain tissues with commensurate high morbidity and mortality, weight loss, and cytokine/chemokine production[37,46]. Therefore, this model is ideal for testing SARS-CoV-2 therapeutics due to its severe disease burden, as compared to other animal models, including mouse-attenuated SARS-CoV-2 in wild-type mice or wild-type SARS-CoV-2 in golden Syrian hamsters, which exhibit milder symptoms. Protection in an animal model with high levels of hACE2, such as the K18-hACE2 mouse model, is thus indicative of the high promise of anti-SARS-CoV-2 antivirals[37]. Murine TMPRSS2 protein contains 492 amino acids and shares 81.4% similarity and 77.3% identity with human TMPRSS2[47] and we confirmed that our lead peptidomimetic N-0385 inhibited murine TMPRSS2 with an IC_{50} of 12.3 ± 1.9 nM.

Intranasal administration has several advantages for the prevention and treatment of SARS-CoV-2 and other viral diseases, including ease of self-administration. SARS-CoV-2 mainly enters the human body through ACE2 and TMPRSS2 positive nasal epithelial cells[48–50]. Intranasal drug delivery maximizes airway and lung exposure while limiting systemic exposure. For example, intranasal administration of a membrane fusion inhibitory lipopeptide prevented transmission of SARS-CoV-2 in ferrets[51]; however, efficacy of intranasal delivery of a small molecule inhibitor has not been shown. Under our conditions, intranasal administration of N-0385 significantly reduced morbidity and mortality in the K18-hACE2 mouse model of severe human COVID-19 pathology. We first investigated the survival benefit of an eight-day N-0385 treatment regimen, which protected 70% of the mice from SARS-CoV-2-induced mortality. Once efficacy was established, we investigated a shortened early treatment regimen and observed 100% survival of these mice, underlining the potent antiviral efficacy of N-0385 and the importance of the TTSP-mediated proteolytic maturation of spike protein for SARS-CoV-2 infection *in vivo*. In addition to the reduced mortality, morbidity, and histological signs, IHC analysis and plaque assays indicated a 98% and 97% reduction in SARS-CoV-2, respectively, in the lungs of N-0385 treated mice 3 dpi. This is indicative of the effective reduction of virus propagation by N-0385 in this animal model. While further studies are needed to understand the ideal time points for N-0385 administration, we demonstrated that N-0385 may also contribute therapeutic efficacy against SARS-CoV-2 VOCs. A single dose at the time of infection or 12 hours after B.1.617.2 infection significantly protected against COVID-19-associated weight loss[37,39], and significantly reduced viral burdens at 3 dpi (>50%), confirming that N-0385 can act as a pan-SARS-CoV-2 prophylactic and therapeutic.

Antiviral candidates for SARS-CoV-2 infection are currently under investigation in clinical trials and in animal models but to date, only one study on the DAA GC-376 has reported protection against lethal SARS-CoV-2 infection in the K18-hACE2 model[26]. Plitidepsin, a newly discovered naturally occurring HDA, protected against lung pathology in the K18-hACE2 model; however, the effect on mortality was not reported[25]. Plitidepsin is a promising HDA, which targets the ubiquitously expressed elongation factor 1-alpha 1 and has demonstrated high potency (EC_{50} = 1.62 nM and SI = 40.4) against SARS-CoV-2 infection in pneumocyte-like cells[25]. Cm and nafamostat mesylate are also HDAs targeting serine proteases, including host TTSPs, that are undergoing human trials against SARS-CoV-2; however, no significant protection against infection was observed in the adenovirus hACE2 model (Cm) of SARS-CoV-2 infection[4,52]. Recently reported clinical trial data for Cm treatment of hospitalized COVID-19 patients demonstrated a lack of impact on time to recovery and incidence of death following SARS-CoV-2 infection[19]. Antivirals will likely need to be administered during the very early phase of COVID-19 to be effective in lowering the risk of disease progression, consistent with our short early treatment regimen in K18-hACE2 mice infected with SARS-CoV-2.

Overall, we have developed and characterized N-0385, a novel highly potent inhibitor of TMPRSS2-like proteases that blocks SARS-CoV-2 VOCs (B.1.1.7, P.1, B.1.351 and B.1.617.2) and is broadly protective against infection and mortality in mice. In addition, we demonstrated that N-0385 provides a novel effective early treatment option against SARS-CoV-2 and the B.1.617.2 Delta VOC. Further, N-0385 analogs may have broader applications in combating other widespread respiratory viruses that usurp TMPRSS2-related proteases for viral entry, including other established coronaviruses, influenza viruses, and additional viruses that depend on TTSPs for entering host cells[4,30,41]. We envision a practical use of N-0385 for unvaccinated individuals or those with high risk of exposure or severe disease outcome related to SARS-CoV-2 VOCs and future emerging pathogens. Practically, TTSP inhibitors should be administered as soon as possible following exposure to SARS-CoV-2 for maximal effect and may possibly act synergistically when used in multi-drug combinations with replication inhibitors such as Remdesivir, Paxlovid, and Molnupiravir to reduce the risk of antiviral resistance mutations.

Online content

Any methods, additional references, Nature Research reporting summaries, source data, extended data, supplementary information, acknowledgements, peer review information; details of author contributions and competing interests; and statements of data and code availability are available at https://doi.org/10.1038/s41586-022-04661-w.

1. Planas, D. et al. Considerable escape of SARS-CoV-2 Omicron to antibody neutralization. *Nature* **2021**, 1–7, https://doi.org/10.1038/s41586-021-04389-z (2021).
2. Tao, K. et al. The biological and clinical significance of emerging SARS-CoV-2 variants. *Nature Reviews Genetics* **2021**, 757–773 (2021). 22:12 22.
3. Shang, J. et al. Cell entry mechanisms of SARS-CoV-2. *PNAS* **117**, 11727–11734 (2020).
4. Hoffmann, M. et al. SARS-CoV-2 Cell Entry Depends on ACE2 and TMPRSS2 and Is Blocked by a Clinically Proven Protease Inhibitor. *Cell* **181**, 271–280.e8 (2020).
5. Wong, J. P. & Damania, B. SARS-CoV-2 dependence on host pathways. *Science (New York, N.Y.)* **371**, 884–885 (2021).
6. Jackson, C. B., Farzan, M., Chen, B. & Choe, H. Mechanisms of SARS-CoV-2 entry into cells. *Nature Reviews Molecular Cell Biology* **2021**, 1–18, https://doi.org/10.1038/s41580-021-00418-x (2021).

7. Rees, W. D. et al. Enteroids Derived From Inflammatory Bowel Disease Patients Display Dysregulated Endoplasmic Reticulum Stress Pathways, Leading to Differential Inflammatory Responses and Dendritic Cell Maturation. *Journal of Crohn's and Colitis* **14**, 948–961 (2020).
8. Zhou, P. et al. A pneumonia outbreak associated with a new coronavirus of probable bat origin. *Nature* **579**, 270–273 (2020).
9. COVID-19 Dashboard by the Center for Systems Science and Engineering (CSSE) at Johns Hopkins University. https://coronavirus.jhu.edu/map.html.
10. Callaway, E. Beyond Omicron: what's next for COVID's viral evolution. *Nature* **600**, 204–207 (2021).
11. Plante, J. A. et al. The variant gambit: COVID-19's next move. *Cell Host and Microbe* **29**, 508–515 (2021).
12. Sievers, B. L. et al. Antibodies elicited by SARS-CoV-2 infection or mRNA vaccines have reduced neutralizing activity against Beta and Omicron pseudoviruses. *Science Translational Medicine* (2022) https://doi.org/10.1126/SCITRANSLMED.ABN7842.
13. Chitalia, V. C. & Munawar, A. H. A painful lesson from the COVID-19 pandemic: the need for broad-spectrum, host-directed antivirals. *Journal of Translational Medicine* **18**, 390 (2020).
14. Murgolo, N. et al. SARS-CoV-2 tropism, entry, replication, and propagation: Considerations for drug discovery and development. *PLoS pathogens* **17**, e1009225 (2021).
15. Kokic, G. et al. Mechanism of SARS-CoV-2 polymerase stalling by remdesivir. *Nature Communications* **12**, 279 (2021).
16. Beigel, J. H. et al. Remdesivir for the Treatment of Covid-19 — Final Report. *New England Journal of Medicine* **383**, 1813–1826 (2020).
17. Owen, D. R. et al. An oral SARS-CoV-2 M pro inhibitor clinical candidate for the treatment of COVID-19. *Science* **374**, 1586–1593 (2021).
18. Wahl, A. et al. SARS-CoV-2 infection is effectively treated and prevented by EIDD-2801. *Nature* 1–9 (2021) https://doi.org/10.1038/s41586-021-03312-w.
19. Gunst, J. D. et al. Efficacy of the TMPRSS2 inhibitor camostat mesilate in patients hospitalized with Covid-19-a double-blind randomized controlled trial. *EClinicalMedicine* **0**, 100849 (2021).
20. Beumer, J. et al. A CRISPR/Cas9 genetically engineered organoid biobank reveals essential host factors for coronaviruses. *Nature Communications* **2021**, 1–12 (2021). 12:1 12.
21. Hoffmann, M., Kleine-Weber, H. & Pöhlmann, S. A Multibasic Cleavage Site in the Spike Protein of SARS-CoV-2 Is Essential for Infection of Human Lung Cells. *Molecular Cell* **78**, 779–784.e5 (2020).
22. Tang, T. et al. Proteolytic Activation of SARS-CoV-2 Spike at the S1/S2 Boundary: Potential Role of Proteases beyond Furin. *ACS Infectious Diseases* **7**, 264–272 (2021).
23. Hoffmann, M. et al. Camostat mesylate inhibits SARS-CoV-2 activation by TMPRSS2-related proteases and its metabolite GBPA exerts antiviral activity. *EBioMedicine* **000**, 103255 (2021).
24. Rathnasinghe, R. et al. Comparison of transgenic and adenovirus hACE2 mouse models for SARS-CoV-2 infection. *Emerging Microbes and Infections* **9**, 2433–2445 (2020).
25. White, K. M. et al. Plitidepsin has potent preclinical efficacy against SARS-CoV-2 by targeting the host protein eEF1A. *Science* **371**, 926–931 (2021).
26. Dampalla, C. S. et al. Postinfection treatment with a protease inhibitor increases survival of mice with a fatal SARS-CoV-2 infection. Proceedings of the National Academy of Sciences of the United States of America (2021) https://doi.org/10.1073/pnas.2101555118.
27. Colombo, É. et al. Design and synthesis of potent, selective inhibitors of matriptase. *ACS Medicinal Chemistry Letters* **3**, 530–534 (2012).
28. Beaulieu, A. et al. Matriptase Proteolytically Activates Influenza Virus and Promotes Multicycle Replication in the Human Airway Epithelium. *Journal of Virology* **87**, 4237–4251 (2013).
29. St-Georges, C. et al. Modulating the selectivity of matriptase-2 inhibitors with unnatural amino acids. *European Journal of Medicinal Chemistry* **129**, 110–123 (2017).
30. Murza, A. et al. Inhibitors of type II transmembrane serine proteases in the treatment of diseases of the respiratory tract–A review of patent literature. *Expert Opinion on Therapeutic Patents* **30**, 807–824 (2020).
31. Shrimp, J. H. et al. An Enzymatic TMPRSS2 Assay for Assessment of Clinical Candidates and Discovery of Inhibitors as Potential Treatment of COVID-19. ACS Pharmacology and Translational. *Science* **3**, 997–1007 (2020).
32. Béliveau, F. et al. Discovery and Development of TMPRSS6 Inhibitors Modulating Hepcidin Levels in Human Hepatocytes. *Cell Chemical Biology* **26**, 1559–1572.e9 (2019).
33. Long, R. K. M. et al. Super resolution microscopy and deep learning identify Zika virus reorganization of the endoplasmic reticulum. *Scientific Reports* **10**, 1–18 (2020).
34. Staab, J. F., Lemme-Dumit, J. M., Latanich, R., Pasetti, M. F. & Zachos, N. C. Co-Culture System of Human Enteroids/Colonoids with Innate Immune Cells. *Current Protocols in Immunology* **131**, e113 (2020).
35. Rees, W. D. et al. Enteroids Derived From Inflammatory Bowel Disease Patients Display Dysregulated Endoplasmic Reticulum Stress Pathways, Leading to Differential Inflammatory Responses and Dendritic Cell Maturation. *Journal of Crohn's and Colitis* **14**, 948–961 (2020).
36. Lamers, M. M. et al. SARS-CoV-2 productively infects human gut enterocytes. *Science* **369**, 50–54 (2020).
37. Winkler, E. S. et al. SARS-CoV-2 infection of human ACE2-transgenic mice causes severe lung inflammation and impaired function. *Nature Immunology* **21**, 1327–1335 (2020).
38. McCray, P. B. et al. Lethal Infection of K18-hACE2 Mice Infected with Severe Acute Respiratory Syndrome Coronavirus. *Journal of Virology* **81**, 813–821 (2007).
39. Johansen, M. D. et al. Animal and translational models of SARS-CoV-2 infection and COVID-19. *Mucosal Immunology* **13**, 877–891 (2020).
40. Cáceres, C. J. et al. Efficacy of GC-376 against SARS-CoV-2 virus infection in the K18 hACE2 transgenic mouse model. *Scientific Reports* **2021**, 1–13 (2021). 11:1 11.
41. Laporte, M. & Naesens, L. Airway proteases: an emerging drug target for influenza and other respiratory virus infections. *Current Opinion in Virology* **24**, 16–24 (2017).
42. Klingenstein, M. et al. Evidence of SARS-CoV2 Entry Protein ACE2 in the Human Nose and Olfactory Bulb. *Cells Tissues Organs* 1–10 (2021) https://doi.org/10.1159/000513040.
43. Lukassen, S. et al. SARS-CoV-2 receptor ACE2 and TMPRSS2 are primarily expressed in bronchial transient secretory cells. *EMBO J* **39**, e105114 (2020).
44. Hatesuer, B. et al. Tmprss2 Is Essential for Influenza H1N1 Virus Pathogenesis in Mice. *PLoS Pathogens* **9**, e1003774 (2013).
45. Mahoney, M. et al. A novel class of TMPRSS2 inhibitors potently block SARS-CoV-2 and MERS-CoV viral entry and protect human epithelial lung cells. *Proceedings of the National Academy of Sciences* **118**, e2108728118 (2021).
46. Lutz, C., Maher, L., Lee, C. & Kang, W. COVID-19 preclinical models: Human angiotensin-converting enzyme 2 transgenic mice. *Human Genomics* **14**, 20 (2020).
47. Soldatov, V. O., Kubekina, M. V., Silaeva, Y. Y., Bruter, A. V. & Deykin, A. V. On the way from SARS-CoV-sensitive mice to murine COVID-19 model. *Research Results in Pharmacology* **6**, 1 (2020).
48. TS, H. et al. Intranasal Antiviral Drug Delivery and Coronavirus Disease 2019 (COVID-19): A State of the Art Review. *Otolaryngology-head and neck surgery: official journal of American Academy of Otolaryngology-Head and Neck Surgery* **163**, 682–694 (2020).
49. Gallo, O., Locatello, L. G., Mazzoni, A., Novelli, L. & Annunziato, F. The central role of the nasal microenvironment in the transmission, modulation, and clinical progression of SARS-CoV-2 infection. *Mucosal Immunology* **14**, 1 (2021).
50. Erdő, F., Bors, L. A., Farkas, D., Bajza, Á. & Gizurarson, S. Evaluation of intranasal delivery route of drug administration for brain targeting. *Brain Research Bulletin* **143**, 155–170 (2018).
51. de Vries, R. D. et al. Intranasal fusion inhibitory lipopeptide prevents direct-contact SARS-CoV-2 transmission in ferrets. *Science* **371**, 1379–1382 (2021).
52. Sun, Y. J. et al. Structure-based phylogeny identifies Avoralstat as a TMPRSS2 inhibitor that prevents SARS-CoV-2 infection in mice. *Journal of Clinical Investigation* (2021) https://doi.org/10.1172/jci147973.

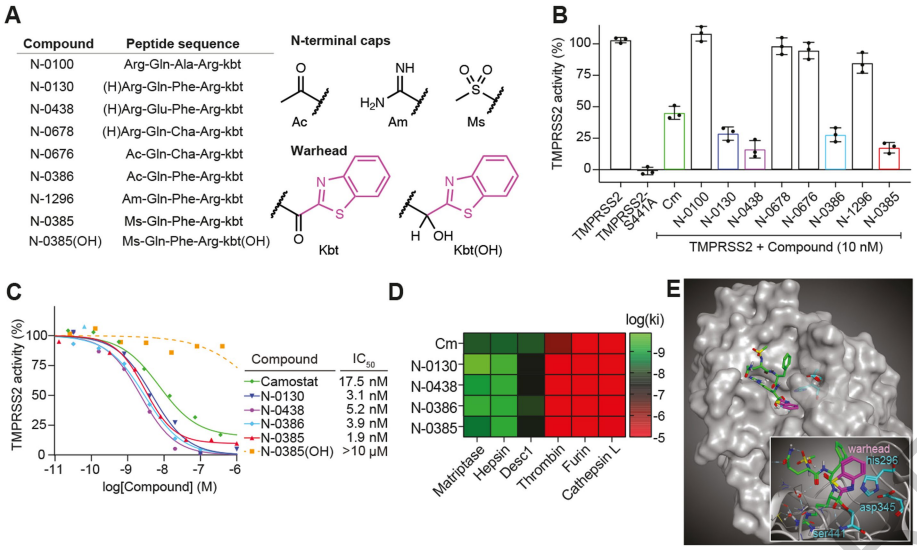

Fig. 1 | Ketobenzothiazole-based peptidomimetics are potent TMPRSS2 inhibitors. (**A**) Peptidomimetic compounds used in this study along with their respective sequences. The structures of N-terminal caps, the ketobenzothiazole warhead, and the alcohol ketobenzothiazole are shown on the right. (**B**) Vero E6 cells were transfected with either an empty vector (mock), TMPRSS2 wild type (WT), or the inactive mutant TMPRSS2-S441A for 24 hr. Indicated compounds (10 nM) were added concomitantly with a fluorogenic substrate on cells for an additional 24 hr before fluorescence reading. Relative TMPRSS2 activity was measured using the mock-subtracted fluorescence and reported as the percentage of residual activity relative to the vehicle-treated cells (0.01% DMSO). Data are presented as mean ± SD (n = 3 independent experiments). (**C**) Dose-response curves were generated for the indicated compounds using the assay described in (**B**), and IC_{50} values were determined using nonlinear regression analysis. Representative IC_{50} curves are shown; the mean value of independent experiments is shown (n=3 for N-0130, N-0386 and N-0385(OH), n = 4 for Cm and N-0385, n = 5 for N-0438). (**D**) Specificity of selected compounds toward other serine proteases is shown. Data are represented as mean of log (K_i), n = 3 independent experiments (except Cathepsin L vs. N-0385, n = 4) and represented as a heat map. (**E**) Large: Docking of N-0385 (green, warhead in purple) in the binding pocket of TMPRSS2 (homology model). Residues of the catalytic triad are shown in cyan. Small: Interaction of N-0385 with TMPRSS2 residues. N-0385 forms a covalent bond with catalytic triad residue Ser441. (H)Arg = desamino arginine, Ac = acetyl, Am = amidinyl, Ms = mesyl, kbt = ketobenzothiazol, Cm = Camostat mesylate, Cha = cyclohexylalanine.

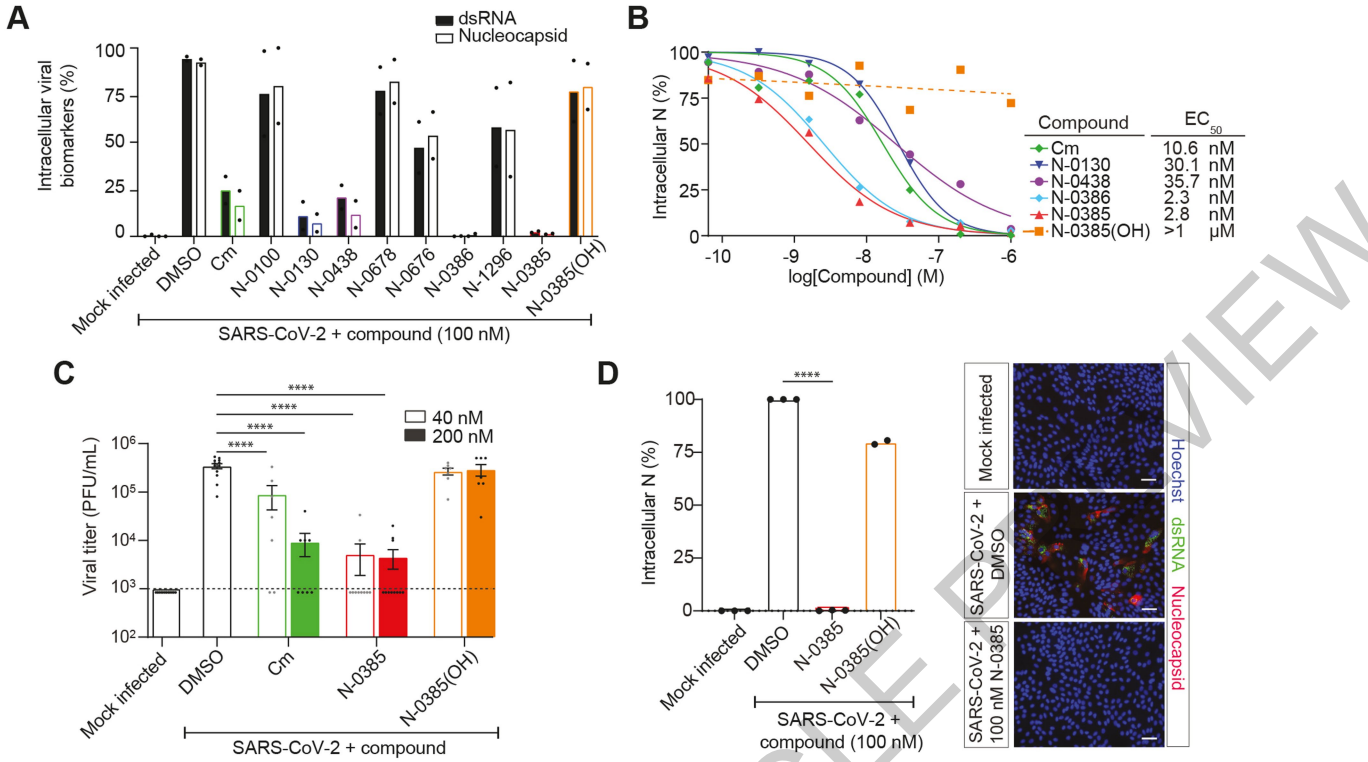

Fig. 2 | Peptidomimetics active against TMPRSS2 are potent low nanomolar inhibitors of SARS-CoV-2 in a human lung epithelial cell line and in human colonoids. **(A)** Calu-3 cells were pretreated with 100 nM of the indicated compounds followed by SARS-CoV-2 infection (MOI = 2). Intracellular infection levels were evaluated by high-content screening of cell nuclei, dsRNA, and nucleocapsid and then quantified relative to DMSO-treated cells (n=2 independent experiments). **(B)** Dose-response curves were generated for the lead antiviral peptidomimetic compounds in Calu-3 cells using nucleocapsid staining of compound pretreated and infected cells (n: Cm = 5, N-0130 = 5, N-0438 = 3, N-0386 = 4, N-0385 = 8, N-0385(OH) = 5). **(C)** Plaque assays were performed using two of the experimental conditions evaluated in the dose-response analysis (40 nM and 200 nM) to determine the viral titers (amount of infectious virus) produced in cells pretreated with the indicated compounds prior to infection (n = 3 independent experiments); dotted line represents limit of detection. **** (modified p <0.0001). **(D)** Colonoids were pretreated with 100 nM of the indicated compounds and infected with SARS-CoV-2 (MOI ≈ 1). Intracellular infection was relatively quantified using nucleocapsid staining. Representative fluorescent images of colonoids subjected to the indicated treatments are shown (Hoechst in blue, nucleocapsid in red, dsRNA in green). Scale bars 50 µm. (N-0385, n = 3; N-038(OH), n = 2); **** modified p <0.0001. One-way ANOVA with Bonferroni correction was used to determine significance in (C) and (D). Error bars represent standard error of the mean. Cm = Camostat mesylate, N = nucleocapsid, PFU = plaque-forming units, MOI = multiplicity of infection.

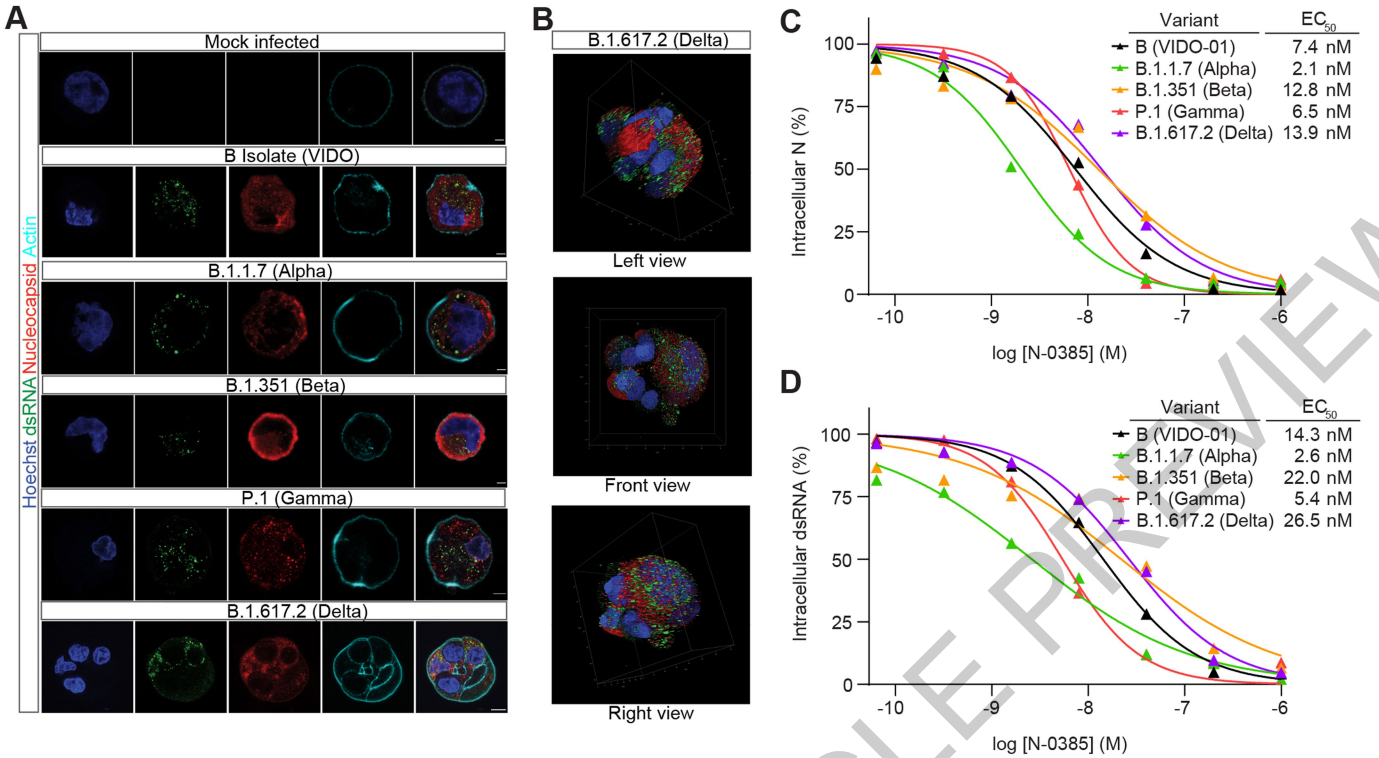

Fig. 3 | N-0385 is a nanomolar inhibitor of four SARS-CoV-2 variants of concern (VOCs). (A) Representative fluorescent images of SARS-CoV-2-infected Calu-3 cells. Calu-3 cells infected with the indicated SARS-CoV-2 variants and mock-infected are shown. Scale bar: 5 µm. Hoechst is shown in blue, nucleocapsid in red, dsRNA in green, and actin in cyan. Images captured with a Leica TCS SP8 3× STED microscope. (**B**) Representative images from a 3D volume rendering of Delta-infected cells. Hoechst is shown in blue, nucleocapsid in red, dsRNA in green, and actin in cyan. Images captured with a Leica TCS SP8 3× STED microscope. **(C and D)** Dose response curves were generated for N-0385 in Calu-3 cells using nucleocapsid staining (**C**) and dsRNA staining (**D**) of N-0385 pretreated cells infected with the indicated VOCs (n = 4 independent experiments).

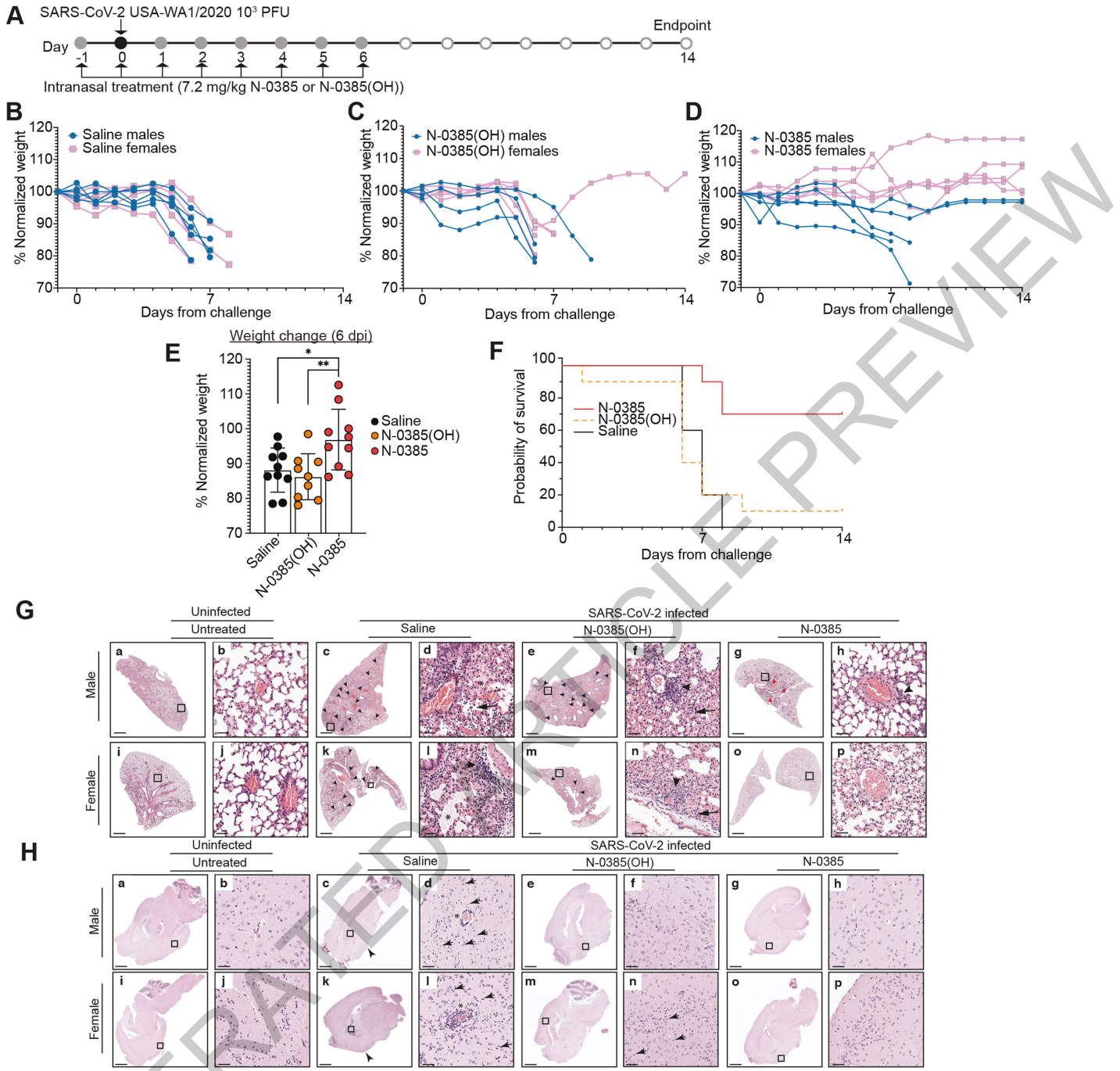

Fig. 4 | N-0385 reduces morbidity and mortality in a SARS-CoV-2 K18-hACE2 mouse model. (A) Mice (n=10 per treatment group) were treated daily on days -1 to +6 relative to infection. Surviving were mice terminated at endpoint. **(B-D)** Weight change of vehicle control, N-0385(OH), and N-0385-treated mice, respectively. **(E)** Weight loss difference at 6 dpi; * p=0.0193, ** p=0.0083. Means ± SD shown, with two-tailed Student's t-tests used to determine significance. **(F)** Survival graph. **(G)** Representative H&E of lung histopathology (one slice analyzed per mouse) at death or study endpoint in mice without treatment (**a-b, i-j**), treated with saline (**c-d**: day 7 and **k-l**: day 6), N-0385(OH) (**e-f**: day 6 and **m-n**: day 6), or N-0385 (**g-h, o-p**: day 14). Uninfected mice tissues (**a-b, i-j**) were normal. Challenged mice (**c-h, k-p**) developed perivascular infiltrates of inflammatory cells (**arrowhead**). Severe inflammatory changes including alveolar fibrin and edema (**asterisk**) were found only in saline group (**c-d, k-l**). Perivascular inflammatory cell infiltrates (**arrowhead**) were more widespread in saline (**c, k**) and control N-0385(OH) (**e, m**) compared to N-0385 mice (**g, o**). Surviving N-0385 mice (**g-h, o-p**) had smaller/fewer perivascular inflammatory infiltrates (**arrowhead**) and occasional type II pneumocyte hyperplasia (**red arrow**). **(H)** Representative H&E images of brain histopathology (one slice analyzed per mouse) in untreated (**a-b, i-j**) and saline treated mice (**c-d**: day 7 and **k-l**: day 8), N-0385(OH) (**e-f**: day 6 and **m-n**: day 7), or N-0385 (**g-h, o-p**: day 14). Saline treated mice (**c-d, k-l**) developed perivascular cuffs of inflammatory cells (**asterisk**), necrotic neurons (**arrow**), gliosis, and meningeal infiltrates (**arrowhead**). Brain lesions were reduced in N-0385(OH) mice (**e-f, m-n**) and absent in surviving N-0385 mice (**g-h, o-p**). Magnified areas were selected to best represent the presence of inflammatory cells and pathological changes. Scale bar **G-H**: **a, c, e, g, i, k, m, o** = 1 mm; **b, d, f, h, j, l, n, p** = 50 µm.

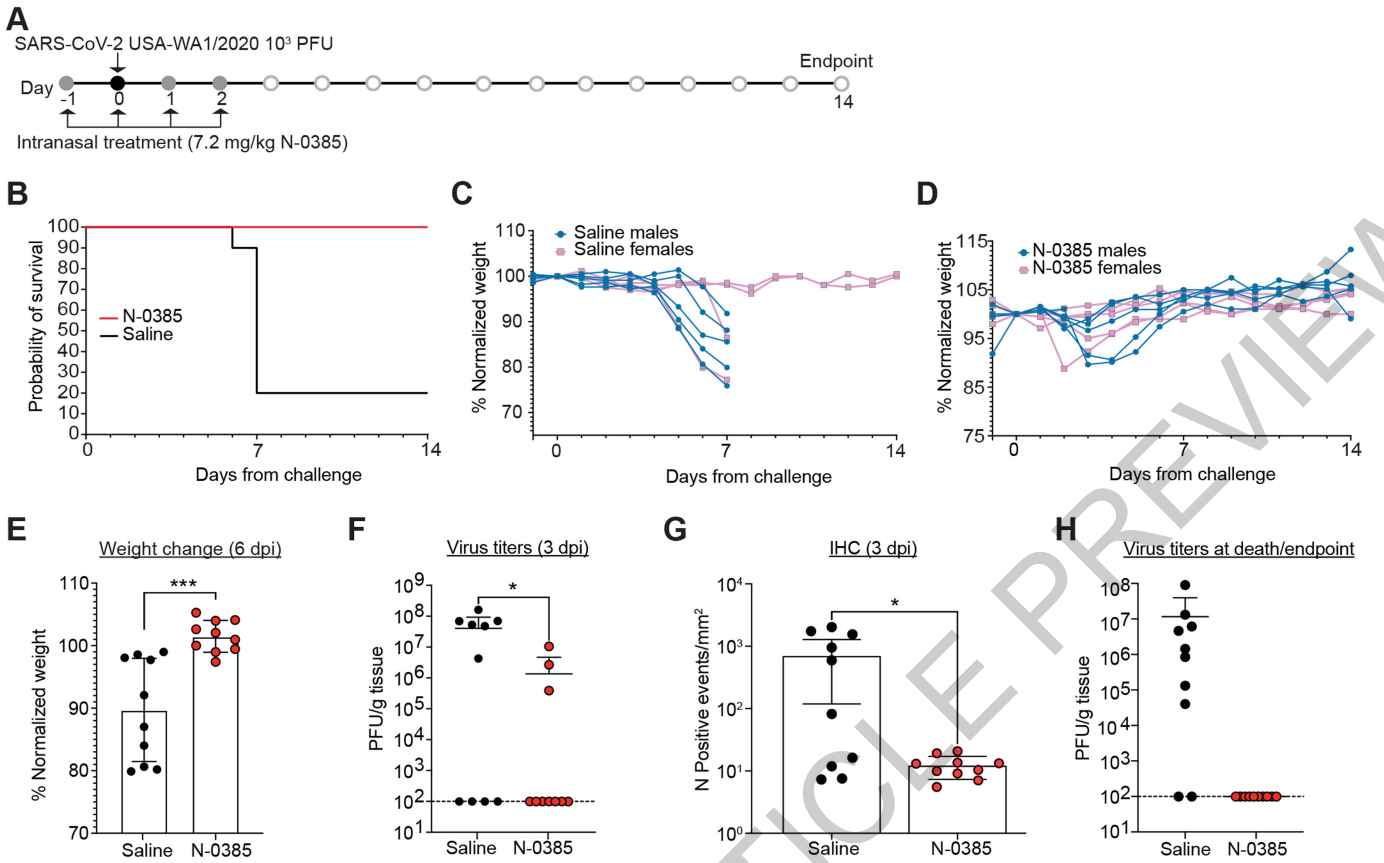

Fig. 5 | N-0385 reduces viral burden, weight loss and completely prevents mortality in a K18-hACE2 mice model of SARS-CoV-2 disease following an early 4-day treatment regimen. (A) K18-hACE2 mice were treated once daily on day -1 to day 2 relative to SARS-CoV-2 infection; surviving mice were terminated on day 14. (**B**) Survival graph. **(C)** Weight change of saline control mice. (**D**) Weight change of N-0385-treated mice. (**E**) Differences in weight loss between treatment groups from **C** and **D** at 6 days post-infection (dpi) [n=10 mice (5 males and 5 females, per group)]. *** p=0.0004. Two-tailed unpaired t-test was used to determine significance. Data presented are mean ± SD. **(F)** Virus titers (plaque forming unit (PFU)/g of tissue) from lungs of infected mice 3 dpi (n=10 mice per group). Titers were significantly lower for the N-0385 group compared to the saline control group; * p=0.0290. Two-tailed Student's t-test used to determine significance. Data presented are mean values ± SD. Plaque assays were performed twice per sample from each mouse and the average used to determine PFU/g. (**G**) Numbers of events/mm^2 that were positive for SARS-CoV-2 nucleocapsid (N) by IHC staining in lung tissue at 3 dpi; reduction in positive cells was significantly greater for the N-0385 vs. saline control; * p=0.0433. Two-tailed Mann Whitney test was used to determine significance. Data are mean ± SD. One complete lung section per mouse was analyzed, n=10 mice per treatment group. (**H**) Virus titers (PFU/g of tissue) from the lungs of infected mice (n = 10 mice per group) at the time of death or study endpoint. Statistical analysis was not performed as samples are from different timepoints. Data are mean ± SD (logarithmic scale precludes negative values to be shown). Plaque assays were performed twice per sample from each mouse and average used to determine PFU/g.

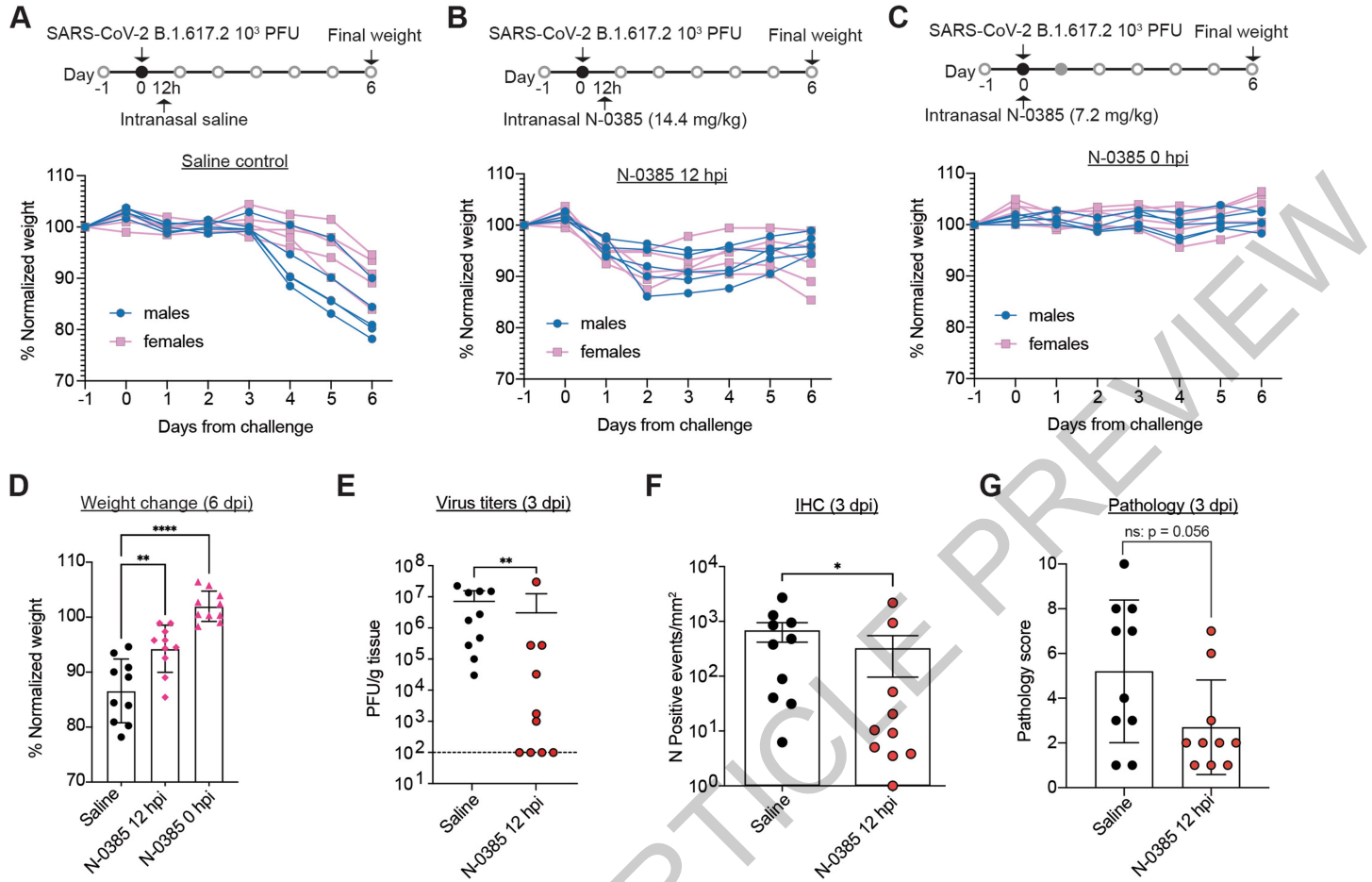

Fig. 6 | N-0385 reduces weight loss and viral burden in K18-hACE2 mice infected with SARS-CoV-2 B.1.617.2 Delta VOC following single dose treatment. **(A)** Weight change in K18-hACE2 mice treated once with saline 12 hr post-infection (hpi). (**B**) Weight change in mice treated once with N-0385 at 12 hpi (14.4 mg/kg). (**C**) Weight change in mice treated once with N-0385 at 0 hpi (7.2 mg/kg). (**D**) Differences in weight loss across three treatment groups **A-C** at 6 dpi (n=10 mice per treatment group); ** p=0.0012; **** p≤ 0.0001. One-way ANOVA using Dunnett's multiple comparisons test used to assess significance. Data presented are mean ± SD. (**E**) Virus titers (plaque forming unit (PFU)/g of tissue) from the lungs of infected mice 3 dpi. Titers were significantly lower for the N-0385 group compared to the saline control group; ** p=0.0081. Two-tailed Mann Whitney test used to determine significance. Data presented are mean values ± SD, n=10 mice per group. Plaque assays were performed twice per sample from each mouse and the average used to determine PFU/g. (**F**) Numbers of events/mm² that were positive for SARS-CoV-2 nucleocapsid (N) by immunohistochemistry (IHC) staining in lung tissue at 3 dpi; reduction in positive cells was significantly greater for the N-0385 vs. saline control; * p=0.0355. Two-tailed Mann Whitney test used to determine significance. Data presented are mean values ± SD, 1 whole lung section was analyzed per mouse (n=10 mice per group) in the study. (**G**) Total lung pathology scores of infected mice 3 dpi as assessed on IHC were improved by approximately 1.9-fold (or 46%) and approach statistical significance; p=0.053. Two-tailed Mann-Whitney test was used to determine significance Data presented are mean values ± SD. One complete lung section per mouse was analyzed, n=10 mice per group.

Methods

Cell lines, antibodies, and inhibitors

Calu-3 cells[54] (ATCC® HTB-55™) were cultivated according to ATCC recommendations. All experiments were performed in these cells below passage 15. Vero E6 cells (ATCC® CRL-1586™; used for SARS-CoV-2 plaque assay) were cultivated in MEM supplemented with 10% FBS, 1 mM sodium pyruvate, and 0.1 nM non-essential amino acids and used at passage <40. All cells were expanded in a T175 flask with 5% carbon dioxide at 37 °C. Cell density was kept between 0.25 and 2 million cells/mL. Vero E6 cells (used for TMPRSS2 proteolytic activity screening and IC_{50} determination) were maintained in Eagle's Minimum Essential Medium (EMEM) containing 10% foetal bovine serum, 2 mmol/L L-glutamine, 100 IU/mL penicillin and 100 lg/mL streptomycin. Camostat mesylate was obtained from MilliporeSigma. The SARS-CoV-2 nucleocapsid antibody [HL344] (GTX635679) was kindly provided by Genetex; mouse anti-dsRNA antibody (J2-1904) was purchased from Scions English and Scientific Consulting[33]; Hoechst 33342 and secondary antibodies goat anti-mouse IgG Alexa Fluor 488 (A11001) and goat anti-rabbit IgG Alexa Fluor 555 (A21428) were obtained from Invitrogen.

Peptidomimetic compound synthesis

Preparation of the compounds using a mixed approach of solution and solid-phase synthesis is described in the supplementary materials, in addition to a synthetic scheme of analogues, NMR, HRMS, UPLC-MS retention time, structure, purity, and molecular formula strings of compounds. Amino acids and coupling reagents were obtained from Chem-Impex International (USA) and used as received. All other reagents and solvents were purchased from Sigma-Aldrich (Canada) or Fisher Scientific (USA). Tetrahydrofuran (THF) was dried over sodium benzophenone ketyl; DCM over P2O5; methanol over magnesium. Celite (AW Standard Super-Cel® NF) was obtained from Sigma-Aldrich (Canada). Thin layer chromatography was carried out on glass plates covered with silica gel (250 µm) 60 F-254 (Silicycle). Flash chromatography was carried out with Silicaflash® P60 (40-63 µm, Silicyle). Chlorotrityl chloride (CTC) resin was obtained from Matrix Innovation and generally used with a loading of 1.2 mmol/g. Reactions on resin were conducted in 60 mL polypropylene cartridges (obtained from Applied Separations) and Teflon stopcocks. Reactors were gently rocked on an orbital shaker at 172 rpm during solid-phase chemistry. The resin was washed with the indicated solvent for 2-5 min with 10 mL solvent per gram of resin. Purity was analyzed on a Waters UPLC H-Class with UV detection PDA equipped with an Acquity UPLC CSH C18 1.7 µm 2.1 x 50 mm^2 column. MS spectra were recorded on a Waters SQD 2 detector (electrospray) instrument with a linear gradient of 5-95% CH_3CN and H_2O containing 0.1% formic acid. Final products were purified to >95% purity (UPLC-UV) using a Waters Preparative LC (Sample Manager 2767 (fraction collector); Binary gradient module 2545, with two 515 HPLC pumps and a system fluidics organizer (SFO); Photodiode Array Detector 2998: column X Select CSH Prep C18 5 µm OBD 19 x 250 mm^2 column; buffer: A: 0.1% HCOOH in H_2O; B: 0.1% HCOOH in ACN; flow 20 mL/min). The gradient was 10-60% of acetonitrile at a flow rate of 20 mL/min. Purities of all compounds in this paper were >95% as assessed by UPLC.

Molecular modeling

A homology model of TMPRSS2 catalytic domain was built using the structure of matriptase (PDB: 6N4T) with the "Homology Model" module of the Molecular Operating Environment (MOE) from the Chemical Computing Group. Sequence alignment of catalytic domains of matriptase with TMPRSS2 using "Align Sequences Protein BLAST" and MOE sequence alignment allowed building of a high-quality model. Ten models were created, and the final model was selected using the best score obtained by the generalized-born volume integral/weighted surface area (GBVI/WSA) scoring method[55]. The final model was refined and minimized using the Amber10:Extended Huckel Theory (EHT) force field. After drawing the structure, all protein-ligand complexes were prepared using the Protonate 3D tool; then the partial charges were calculated, and the ligands were energy-minimized.

Molecules were docked in the protein-binding site with the software MOE2019.01.02. All atoms were fixed, and the ligands were allowed to be flexible. The carbon of the ketone making the reversible covalent bond with the protein was fixed at 3.0 ± 0.1 Å of the catalytic serine to constrain the position of the ketobenzothiazole group within the binding site. The guanidine of the Arg in P1 was also fixed via two key interactions in the binding site. Conformational search using LowModeMD was made with AMBER10:EHT as a molecular mechanics force field with default parameters (rejection limit: 100; RMS gradient: 0.05; conformation limit: 10000; iteration limit: 10000). Finally, a second round of energy minimization was performed around the ligand-binding site. The low energy conformations of the inhibitor-protein complexes were analysed for their binding interactions.

TMPRSS2 pericellular activity screening assay and IC_{50} determination

Vero E6 cells were transfected with mock (pcDNA3.1), TMPRSS2 (pcDNA3.1/TMPRSS2 Uniprot: O15393-1), or TMPRSS2-S441A (pcDNA3.1/TMPRSS2-S441A) using Lipofectamine 3000 (ThermoFisher) in 12-well plates. For the mouse TMPRSS2 assay, empty vector (pCMV6-Entry, Origene #PS100001) and TMPRSS2-Myc-DDK (Origene: #MR207852) were used. After 24 hr transfection, cells were washed with PBS and media replaced with HCell-100 media (Wisent) containing 200 µM Boc-QAR-AMC (R&D Systems) and either vehicle (0.01% DMSO) or compounds at the indicated concentration for 24 hr. To measure proteolytic activity, 90 µL of cell media was transferred to a black 96-well plate, and fluorescence was measured at room temperature (excitation: 360 nm, emission: 460 nm) using an FLx800 TBE microplate reader (Bio-Tek Instruments). Background subtracted (mock-transfected cells) proteolytic activities are presented as percentage of activity relative to vehicle-treated cells (screen at 10 nM). IC_{50} values were determined after generating a nonlinear regression analysis from a log([Compound]) vs. a proteolytic activity plot using GraphPad Prism software (version 9.0.1). GraphPad Prism was used to identify and eliminate outliers (Q = 1) and assess the goodness of the fits. IC_{50} values presented are the mean ± standard deviation (SD) of at least three independent experiments.

SARS-CoV-2 infection and treatment in Calu-3 lung epithelial cells

All infections were carried out in a Biosafety Level 3 (BSL3) facility (UBC FINDER) in accordance with the Public Health Agency of Canada and UBC FINDER regulations (UBC BSL3 Permit # B20-0105 to FJ). SARS-CoV-2 (SARS-COV-2/Canada/VIDO-01/2020) was kindly provided by Dr. Samira Mubareka (Sunnybrook, ONT, Canada). SARS-CoV-2 VOCs (B.1.1.7, B.1.351, P.1 and B.1.617.2) were kindly provided by Dr. Mel Krajden (BC Centre for Disease Control, BC, Canada). SARS-CoV-2 VOCs were first isolated in Vero-TMPRSS2 cells (passage 1) and then passaged in Vero E6 cells (passage 2). Viral stocks used in the experiments (passage 3) were propagated in Vero E6 cells[56]. For experiments, passage three of the virus was used with a determined viral titer of 1.5×10^7 plaque-forming units (PFU)/mL. Calu-3 cells were seeded at a concentration of 10,000 cells/well in 96-well plates the day before infection. SARS-CoV-2 stocks were diluted in cell-specific media to a multiplicity of infection (MOI) of 2. Cells were pretreated with compounds for 3 hr and then incubated with the virus for 2 days, followed by fixation of the cells with 3.7% formalin for 30 min to inactivate the virus. The fixative was removed, and cells were washed with PBS, permeabilized with 0.1% Triton X-100 for 5 min, and blocked with 1% Bovine serum albumin (BSA) for 1 hr, followed by immunostaining with the mouse primary antibody J2 (dsRNA) and rabbit primary antibody HL344 (SARS-CoV-2 nucleocapsid) at working dilutions of 1:1000 for 1 hr at room temperature. Secondary antibodies were used at a 1:2000 dilution and included the goat anti-mouse IgG Alexa Fluor 488 and goat anti-rabbit IgG Alexa Fluor

555 with the nuclear stain Hoechst 33342 at 1 µg/mL and F-actin staining with Alexa Fluor 647 phalloidin at a 1:300 dilution for 1 hr at room temperature in the dark. After washing with PBS, plates were kept in the dark at 4 °C until imaging on a high-content screening (HCS) platform (Cellinsight CX7 HCS, Thermo Fisher Scientific) with a 10X objective, or an EVOS™ M7000 Imaging System (Thermo Fisher Scientific) with a 20X or 40X objective. Confocal imaging was performed with a Leica TCS SP8 STED 3× laser scanning confocal microscope (Leica, Wetzlar, Germany) equipped with a 100×/1.4 Oil HC PL APO CS2 STED White objective, 405nm laser, a white light laser, HyD detectors, and operated with a Leica Application Suite X (LAS X) software. 3D volume rendering was done with LAS-X. 2D Images were exported into tiff format. Merging of different channels and the addition of the scale bar were performed using ImageJ/FIJI.

High-content screening of SARS-CoV-2 infection

Monitoring of the total number of cells (based on nuclei staining) and number of virus-infected cells (based on dsRNA and nucleocapsid staining) was performed using the Cellinsight CX7 HCS platform (Thermo Fisher), as previously described[57,58]. Briefly, nuclei are identified and counted using the 350/461 nm wavelength (Hoechst 33342); cell debris and other particles are removed based on a size filter tool. A region of interest (ROI, or "circle") is then drawn around each host cell and validated against the bright field image to correspond with host cell membranes. The ROI encompasses the "spots" where dsRNA (485/521 nm wavelength) and SARS-CoV-2 nucleocapsid (549/600 nm wavelength) are localized. Finally, the software (HCS Studio Cell Analysis Software, version 4.0) identifies, counts, and measures the pixel area and intensity of the "spots" within the "circle." The fluorescence measured within each cell (circle) is then added and quantified for each well. The total circle spot intensity of each well corresponds to intracellular virus levels ($Z' > 0.7$) and is normalized to non-infected cells and to infected cells with 0.1% DMSO. Nine fields were sampled from each well. Nuclei stain (Hoechst 33342) was also used to quantify cell loss (due to cytotoxicity or loss of adherence) and to verify that the changes in viral infection did not result from a decrease in cell numbers.

Median half-maximal effective concentration (EC_{50}) curves

Intracellular dose response (EC_{50} values) for selected compounds against SARS-CoV-2 were determined by pre-treating Calu-3 cells for three hr with serially diluted compounds (0.064, 0.32, 1.6, 8, 40, 200, and 1000 nM), followed by SARS-CoV-2 infection for 48 hr. Viral infection was detected by staining for dsRNA or nucleocapsid signal and quantified as described above. EC_{50} experiments were repeated at least three times for each compound with three technical replicates in each experiment. Intracellular nucleocapsid levels were interpolated to negative control (0.1% DMSO, no infection) = 0 and positive control (0.1% DMSO, with infection) = 100. The GraphPad Prism 9™ (GraphPad Software, Inc.) nonlinear regression fit modeling variable slope was used to generate a dose-response curve [Y = Bottom + (Top-Bottom)/(1+10^((LogIC$_{50}$-X)*HillSlope)], constrained to top = 100, bottom = 0.

SARS-CoV-2 plaque assay

A total of 250,000 Vero E6 cells were seeded in complete MEM medium in 6-well plates and incubated for 24 hr at 37 °C prior to infection with a 1:1000 dilution of supernatant from mock, infected, and treated and infected cells. The wells were washed once with PBS before 100 µL virus dilution was added per well in quadruplicate. Infected cells were incubated at 37 °C for 1 hr, mixed gently every 15 min, then covered with 2 mL overlay medium of 2% Avicel CL-611 (DuPont Pharma Solutions) or 0.6% agar diluted 1:1 with 2x minimum essential media (Gibco). The cells were then incubated for 3 days. To fix the cells, 2 mL 8% formalin or 4% PFA was added to each well for 30 min, following removal of the overlay/formalin solution. Cells were gently washed with 1 mL tap water/well, followed by staining with 200 µL 1% crystal violet in 20 % methanol for 5 min or in 0.5% crystal violet in 30% methanol for 15 minutes. Crystal violet was removed, and the cells were washed three times with 1 mL tap water/well, then dried before the viral plaques were manually counted.

Cytotoxicity assays

Calu-3 and Vero E6 cells (2500 or 10,000 cells for samples, 80-20,000 cells for standard curve) were seeded in 96-well plates. Following a 24-hr incubation at 37 °C, 5% CO_2, cells were washed with D-PBS and compounds added (10 µM) for an additional 24-hr incubation. Cellular viability was assessed using Cell Titer-Glo® 2.0 Cell Viability Assay (Promega) according to the manufacturer's instructions. The number of viable cells was extrapolated using the standard curve. Cellular viability in Vero E6 cells was expressed relative (%) to vehicle-treated cells. Data are from four independent experiments (mean ± SD).

Protease selectivity of N-0385

Recombinant human matriptase, hepsin, and DESC1 were expressed and purified as described previously[59,60]. Recombinant human furin, human cathepsin L (Bio-techne), and human thrombin (MilliporeSigma) were obtained from commercial sources. Dissociation constants (K_i) were determined using steady-state velocities as previously reported[27,29]. Assays were performed at room temperature in assay buffers (50 mM Tris-HCl pH 7.4; 150 mM NaCl; 500 µg/ml BSA for matriptase, hepsin, DESC1, and thrombin; 50 mM HEPES pH 7.4, 1 mM β-mercaptoethanol, 1 mM $CaCl_2$, 500 µg/ml BSA for furin; 50 mM MES pH 6, 5 mM DTT, 1 mM EDTA, 0.005% Brij 35, 500 µg/ml BSA for Cathepsin L). To measure proteolytic activity, protease (0.25 to 1 nM) was added to the assay buffer containing different concentrations of compounds and a fluorogenic substrate (Boc-RVRR-AMC for furin, Z-LR-AMC for cathepsin L, and Boc-QAR-AMC for the other proteases). Activity was monitored (excitation: 360 nm; emission: 460 nm) using a FLx800 TBE microplate reader (Bio-Tek Instruments). If substantial inhibition occurred using a ratio $I/E \leq 10$ plots of enzyme velocity as a function of the inhibitor, concentrations were fitted by nonlinear regression analysis to the Morrison equation for tight-binding inhibitors. If inhibition occurred only at $I/E > 10$, plots of enzyme velocity as a function of substrate concentration at several inhibitor concentrations were fitted by nonlinear regression to equations describing different models of reversible inhibition (competitive, uncompetitive, non-competitive, and mixed model). The preferred model was used for K_i determination. K_i was calculated from at least three independent experiments (mean ± SD). The maximum concentration of compounds used for the assays was 10 µM.

SARS-CoV-2 infection of human biopsy-derived colonoid monolayers

Intestinal biopsy-derived colonoids from healthy donors were obtained from the Johns Hopkins Conte Digestive Disease Basic and Translational Research Core Center (NIH NIDDK P30-DK089502) and grown according to Staab et al.[34]. Briefly, human colonoid monolayers were generated by combining the colonoids from one Matrigel dome (~100 or more colonoids in a 25 µL dome). Domes were dislodged with a cell scraper in 1 mL of Cultrex Organoid Harvesting solution (Bio-techne, R&D Systems brand, 3700-100-01) and incubated for 1 hr at 4 °C on a shaker at 250 rpm. After incubation, cells were diluted with an equal volume of complete media without growth factors (CMGF; Advanced DMEM/F-12 (Gibco brand, Thermo Fisher Scientific 123634010), 10 mM HEPES (Invitrogen 15630-080), GlutaMAX (Gibco brand, 35050-061), and 100 U/mL of penicillin-streptomycin (Gibco brand, 15140-122)), and then centrifuged at 400 x g for 10 min at 4 °C. Cells were resuspended in 50 µL/well of TrypLE Express (Invitrogen, 12604021) and then incubated for 1 min at 37 °C. Following incubation, 10 mL of cold CMGF was added and the cells were pelleted by centrifugation as above and then resuspended in 100 µL per well of monolayer media (IntestiCult™ Organoid Growth Medium (Human) 06010), 10 µM of Rho Kinase inhibitor, Y-27632 (Stemcell 72304), and 50 µg/mL of gentamicin

(Gibco brand, Thermo Fisher Scientific, 1510064)). They were then seeded at a 1:4 dome-to-well ratio in a 96-well plate coated in 100 µL of 34 µg/mL human collagen IV (Sigma C5533). Cells were fed every 2 days and were used for experiments after they were fully confluent (4-5 days). Cells were treated with compounds for 3 hr prior to SARS-CoV-2 infection (SARS-COV-2/Canada/VIDO-01/2020; MOI ≈ 1) for 72 hr, and then were fixed and stained for nucleocapsid and dsRNA as described above in '*SARS-CoV-2 infection and treatment in Calu-3 lung epithelial cells*'. Quantification of infected cells was performed as described above in '*High-Content Screening of SARS-CoV-2 infection*'. Imaging was performed on the EVOS M7000 microscope using the following channels: 357/447nm for nuclear staining (Hoechst 33342), 470/525nm for dsRNA (Alexa Fluor 488), and 531/593nm for nucleocapsid (Alexa Fluor 555).

Real-time PCR

Total RNA extractions in Calu-3 cells were performed using TRIzol (Invitrogen) with chloroform as recommended by the manufacturer's protocol. The aqueous layer was recovered, mixed with 1 volume of 70% ethanol, and applied directly to an RNeasy Mini kit column (Qiagen). RNA quality and the presence of contaminating genomic DNA were verified as described previously[61]. RNA integrity was assessed with an Agilent 2100 Bioanalyzer (Agilent Technologies). Reverse transcription was performed on 1.1 µg of total RNA with Transcriptor reverse transcriptase, random hexamers, dNTPs (Roche Diagnostics), and 10 units of RNaseOUT (Invitrogen) following the manufacturer's protocol in a total volume of 10 µL. For colonoids, cells were rinsed in ice-cold PBS and lysed using miRNeasy Mini Kit (Qiagen) per manufacturer's instructions. RNA was isolated and reverse-transcribed using Quanta Biosciences qScript cDNA SuperMix.

For the qPCR assays, primers were individually resuspended to 20–100 µM stock solutions in Tris-EDTA buffer and diluted as a primer pair to 1 µM in RNase DNase-free water. qPCRs were performed in 10 µL in 96-well plates on a CFX OPUS-96 thermocycler (Bio-Rad) with 5 µL of 2X PerfeCTa® SYBR® Green Supermix (Quantabio), 10 ng (3 µL) of cDNA, and 200 nM (final concentration; 2 µL) primer pair solutions. The following cycling conditions were used: 3 min at 95 °C and 50 cycles of 15 s at 95 °C, 30 s at 60 °C, and 30 s at 72 °C. Relative expression levels were calculated according to the qBASE framework[62] with YWHAZ, PUM1, and MRPL19 as housekeeping genes for normalization. Primer design and validation were evaluated as described elsewhere[61]. In every qPCR run, a no-template control was performed for each primer pair; these were consistently negative. All qPCR assays were performed by the RNomics Platform of the Université de Sherbrooke.

SARS-CoV-2 infection and treatment in mice

Animal studies were carried out in accordance with the recommendations in the *Guide for the Care and Use of Laboratory Animals* of the National Institutes of Health. All protocols were performed under approved BSL-3 conditions and approved by the Institutional Animal Care and Use Committee at Cornell University (IACUC mouse protocol # 2017-0108 and BSL3 IBC # MUA-16371-1). Intranasal virus and antiviral treatments were performed under anesthesia, and all efforts were made to minimize animal suffering. Eight-week-old heterozygous K18-hACE2 c57BL/6J mice (strain: 2B6.Cg-Tg(K18-hACE2)2Prlmn/J)[38,63,64] were used for this study (Jackson Laboratory, Bar Harbor, ME). Mice were intranasally inoculated with $1x10^3$ PFU/animal using passage 1 of single-plaque isolated virus propagated in Vero-TMPRSS2 cells from isolate USA-WA1/2020 (BEI resources; NR-52281) or isolate NYI31-21 (B1.617.2 Delta VOC) isolated by Dr. Diel's lab at Cornell University. Mice were housed in groups of five per cage and fed a standard chow diet. Daily treatments were administered intranasally at 7.2 mg/kg or 14.4 mg/kg using the average weights of each group separated by sex. Mice were monitored and weighed daily and humanely euthanized at predetermined criteria to minimize distress following approved protocols, generally when weight loss reached 20% from day of challenge or mice became moribund with a clinical score >3 on a 5-point scale[65]. Mouse lungs and brains were collected directly after euthanasia and placed in DMEM with 2% FBS for plaque assays[65]. For each experiment, 10 mice (5 males and 5 females) were used per treatment group, for determination of statistical significance and gender trends. Mice were designated into groups randomly to reduce bias due to differences in weight, and animal studies were performed using age matched mice to compare across groups. Investigators were not blinded to groups during weighing and scoring of animal health due to the nature of the infectious agent.

Mice histopathology

For histologic examination, mouse lungs and brains were collected directly after euthanasia and placed in 10% formalin for >72 hrs after which tissues were embedded in paraffin. Tissue sections (4 µm) were analyzed after staining with H&E and scored blinded by an anatomic pathologist. For lung, scores were applied based on the percentage of each tissue type (alveolus, vessels, etc.) affected using the following criteria: (0) normal; (1) <10% affected; (2) 10-25% affected; (3) 26-50% affected; and (4) >50% affected[66]. Assessment of lung pathology in K18-hACE2 mice infected with SARS-CoV-2 B.1.617.2 Delta VOC following single dose treatment was performed on immunohistochemistry sections counterstained with hematoxylin. For brains, histologic scoring was assessed for perivascular inflammation using the most severely affected vessel and the following criteria: (0) no perivascular inflammation; (1) incomplete cuff one cell layer thick; (2) complete cuff one cell layer thick; (3) complete cuff two to three cells thick; and (4) complete cuff four or more cells thick. Necrotic cells in the neuroparenchyma were assessed per 0.237 mm^2 field using the most severely affected area and the following criteria: (0) no necrotic cells; (1) rare individual necrotic cells; (2) fewer than 10 necrotic cells; (3) 11 to 25 necrotic cells; (4) 26 to 50 necrotic cells; and (5) greater than 50 cells.

To detect viral antigen, sections were labeled with anti-SARS-CoV-2 nucleocapsid protein rabbit IgG monoclonal antibody (GeneTex; GTX635679) at 1:5000 dilution and processed using a Leica Bond Max automated IHC stainer. Leica Bond Polymer Refine Detection (Leica; DS9800) with DAB was used as the chromogen. Image acquisition was performed using a Roche Ventana DP200 slide scanner. Digital image analysis was performed using QuPath software version 0.2.3[67,68]. Tissues were annotated to include all available lung tissue or all brain tissue excluding cerebellum, as cerebellar tissue was not available for all mice. Following annotation, automated detection was performed using automated SLIC superpixel segmentation with a DAB mean detection threshold of 0.18892.

For each experiment, 10 mice (5 males and 5 females) were analyzed per treatment group, for determination of statistical significance and gender trends. Representative images were selected based on the prevalent trend for a given treatment group, showing images representative of the mean pathological score.

Reporting summary

Further information on research design is available in the Nature Research Reporting Summary linked to this paper.

Data availability

All data generated or analysed during this study are included in this published article (and its supplementary and source information files). Correspondence and material requests related to cell-based SARS-CoV-2 studies should be addressed to Dr. François Jean, those related to peptidomimetics and *in vitro* studies should be addressed to Dr. Richard Leduc, and those related to animal studies should be addressed to Dr. Hector C. Aguilar. Source data are provided with this paper.

53. Sarret, P. Éric Marsault (1971–2021): A Legacy through the Prism of Relationship Chemistry. *Journal of Medicinal Chemistry* (2021) https://doi.org/10.1021/acs.jmedchem.1c00481.
54. Shen, B. Q., Finkbeiner, W. E., Wine, J. J., Mrsny, R. J. & Widdicombe, J. H. Calu-3: A human airway epithelial cell line that shows cAMP-dependent Cl- secretion. *American Journal of Physiology* **266**, L493–501 (1994).
55. Corbeil, C. R., Williams, C. I. & Labute, P. Variability in docking success rates due to dataset preparation. *Journal of Computer-Aided Molecular Design* **26**, 775–786 (2012).
56. Ogando, N. S. et al. SARS-coronavirus-2 replication in Vero E6 cells: Replication kinetics, rapid adaptation and cytopathology. *Journal of General Virology* **101**, 925–940 (2020).
57. Shapira, T. et al. High-Content Screening of Eukaryotic Kinase Inhibitors Identify CHK2 Inhibitor Activity Against Mycobacterium tuberculosis. *Frontiers in Microbiology* **11**, 553962 (2020).
58. Olmstead, A. D., Knecht, W., Lazarov, I., Dixit, S. B. & Jean, F. Human Subtilase SKI-1/S1P Is a Master Regulator of the HCV Lifecycle and a Potential Host Cell Target for Developing Indirect-Acting Antiviral Agents. *PLoS Pathogens* **8**, e1002468 (2012).
59. Désilets, A., Longpré, J. M., Beaulieu, M. È. & Leduc, R. Inhibition of human matriptase by eglin c variants. *FEBS Letters* **580**, 2227–2232 (2006).
60. Béliveau, F., Désilets, A. & Leduc, R. Probing the substrate specificities of matriptase, matriptase-2, hepsin and DESC1 with internally quenched fluorescent peptides. *FEBS Journal* **276**, 2213–2226 (2009).
61. Brosseau, J.-P. et al. High-throughput quantification of splicing isoforms. *RNA* **16**, 442–449 (2010).
62. Hellemans, J., Mortier, G., De Paepe, A., Speleman, F. & Vandesompele, J. qBase relative quantification framework and software for management and automated analysis of real-time quantitative PCR data. *Genome Biology* **2007**, 1–14 (2007). 8:2 8.
63. Oladunni, F. S. et al. Lethality of SARS-CoV-2 infection in K18 human angiotensin-converting enzyme 2 transgenic mice. *Nature Communications* **11**, 1–17 (2020).
64. Zheng, J. et al. COVID-19 treatments and pathogenesis including anosmia in K18-hACE2 mice. *Nature* **589**, 603–607 (2021).
65. Burkholder, T., Foltz, C., Karlsson, E., Linton, C. G. & Smith, J. M. Health Evaluation of Experimental Laboratory Mice. *Current Protocols in Mouse Biology* **2**, 145–165 (2012).
66. Meyerholz, D. K. & Beck, A. P. Histopathologic Evaluation and Scoring of Viral Lung Infection. *Methods in Molecular Biology* **2099**, 205–220 (2020).
67. Achanta, R. et al. SLIC superpixels compared to state-of-the-art superpixel methods. *IEEE Transactions on Pattern Analysis and Machine Intelligence* **34**, 2274–2281 (2012).
68. Bankhead, P. et al. QuPath: Open source software for digital pathology image analysis. *Scientific Reports* **7**, 1–7 (2017).

Acknowledgements The authors acknowledge the support of the CL-3 facility (Facility for Infectious Disease and Epidemic Research (FINDER) of the Life Sciences Institute of the University of British Columbia founded by Dr. François Jean and its biosafety support staff including Dr. Bintou Ahidjo (FINDER Research Platform Manager; Honorary Assistant Professor, University of British Columbia) and T. Dean Airey (FINDER Senior Research Technician). We thank the LSI imaging facility of the Life Sciences Institute of the University of British Columbia funded by the Canadian Foundation of Innovation and BC Knowledge Development Fund as well as a Strategic Investment Fund (Faculty of Medicine, University of British Columbia). We further thank Dr. Alex Ball, Jr., MD, Senior Scientist (Genetex), for supplying the SARS-CoV-2 (COVID-19) nucleocapsid antibody [HL344] (GTX635679). We also thank Dr. Samira Mubareka, (Sunnybrook Health Sciences Centre and Research Institute, University of Toronto) for providing the SARS-CoV-2 (SARS-COV-2/Canada/VIDO-01/2020) and Dr. Martin Petric, Samantha Kaweski, Dr. Paul Levett, and Dr. Mel Krajden (BC Centre for Disease Control, BC, Canada) for isolating and providing the SARS-CoV-2 VOCs (B.1.1.7, B.1.351, P.1 and B.1.617.2). We also acknowledge a donation towards the purchase of the CellInsight CX7 HCS system provided by the Vancouver General Hospital Foundation to Dr. Jean, and we thank Dr. Neil Durso for CX7 expertise and support. The authors also acknowledge the support of the Cornell BSL-3, animal, and biosafety support staff and members of the Avery August lab for their support in setting up the animal studies, including but not limited to Amie L. Redko, Nicole Kushner, Paul Jennette, Joshua Turse, Bhupinder Singh, Donna Miller, David G. Collins, and Timothy Lynn Van Deusen. The authors acknowledge the support of NEOMED/adMare in the early phases of developing host-based antivirals. We also acknowledge Ellie Tan for help growing and preparing cells for plaque assays. We also acknowledge Eloic Colombo and Baptiste Plancq for the synthesis of some intermediates, analogs, and warhead. We also recognize the help of the RNomics Platform of the Université de Sherbrooke. We also thank Dr. Jill Kelly for proofreading the manuscript. We thank Dr. Nicholas Zachos from John Hopkins University for providing human colonoids and to the patients who donated these samples for research. The authors dedicate this work to the memory of Professor Eric Marsault[53] (https://doi.org/10.1021/acs.jmedchem.1c00481). **Funding:** This work was supported by operating grants from the Canadian 2019 Novel Coronavirus (COVID-19) Rapid Research Funding program of the Canadian Institutes of Health Research (CIHR) [UBR 322812; VR3-172639 (RL, PLB, and FJ) and OV3-170342 (FJ)]; by a Genome British Columbia / COVID-19 Rapid Response Funding Initiative [COV011 (FJ)]; by the Coronavirus Variants Rapid Response Network [175622 (FJ and AO)]; by a Cornell University Seed Grant, Cornell University start-up funds and a George Mason University, Mercatus Center; Emergent Ventures—Fast Grant (HAC); by a National Institutes of Health research grant [R01AI35270 (GW)]; by a MITACS Accelerate Fellowship [IT18555 (WR)]; an NIH training grant [T32EB023860 (AA to support DWB) and R25GM125597 (AA to support BI)], by an NIH R01 [AI138570 (AA)]; by a CIHR Frederick Banting and Charles Best Canada Graduate Scholarship Award [167018 (SPD)]; by a PROTEO graduate scholarship (TV); and by a MITACS Inc. Accelerate fellowship COVID-19 Award [IT18585 (TS)].

Author contributions S.P.D., D.W.B., B.I. and A.D.O. contributed equally to this work. R.L. and F.J. conceptualized the initiation of the study. F.J. and T.S. conceptualized the cell-culture based SARS-CoV-2 infection experiments; T.S. performed all cell-based SARS-CoV-2 infection experiments, including plating, treating, fixing, staining and scanning cells; T.S. prepared viral stocks of SARS-CoV-2 and variants of concern used in cell-based experiments, performed plaque assays, and quantified viral titers; T.S. performed all the antiviral screening and ED_{50} determination experiments in Calu-3 cells; C.A.H.T. also plated cells (for dose-response curves, confocal imaging, viral propagation, and plaque assays), treated cells with compounds, stained cells for CX7 and confocal microscopy, and scanned plates on CellInsight CX7; W.D.R. prepared colonoids for SARS-CoV-2 infection; H.A.C. and I.A.M. conceptualized the animal experiments; I.A.M. prepared the WA1/2020 virus used in plaque assays and animal experiments, and performed the animal experiments, collected samples for and generated the data in Figs. 4, 5, 6E–G, and Extended Data Fig. 5; M.J. performed all the histopathology and immunohistochemistry analysis; D.W.B. and B.I. performed the plaque assays for Fig. 5F, H and Extended Data Fig. 5C, and the animal experiments for Fig. 6A–D; M.M. and D.G.D. isolated and prepared the virus stock of SARS-CoV-2 B.1.617.2 for use in the animal experiments in Fig. 6; J.S. and A.A. maintained and provided hACE2-K18 mice for the studies used in Fig. 5; T.V. and P.L.B. performed the synthesis of the peptidomimetic compounds; P.L.B. designed the peptidomimetic compounds, coordinated the synthesis and structure-activity relationship studies, and performed molecular modeling; S.P.D. performed all the inhibitor screening and IC_{50} determination experiments in VeroE6 cells; A.D. performed viability assays in Vero E6 cells and in vitro selectivity of N-0385 (K_i); Visualizations and figures were made by T.S., A.O., S.P.D., A.D., G.G., A.C., P.L.B., I.A.M., M.J.; Funding was obtained by R.L., F.J., H.C.A., G.R.W., A.A., E.M., I.R.N., A.O.; A.D., A.O., and P.L.B. contributed to project administration; A.O. coordinated writing, assembly, submission, and revisions of the manuscript; the research was performed under the supervision of F.J., R.L., H.C.A., P.L.B., G.R.W., E.M., A.A., G.R.VdW, D.G.D, I.R.N.; the original manuscript was written by A.O., F.J., P.L.B., R.L., A.D., H.C.A., I.A.M., M.J.; editing and review of the manuscript was performed by T.S., I.A.M., B.I., S.P.D., G.R.W., R.L., P.L.B., A.D., H.C.A., A.C., I.A.M., G.R.VdW., A.A., M.J., I.R.N., A.O., F.J.

Competing interests P.L.B. and R.L. are inventors on patent applications (US9365853B2 and US10988505B2) that cover matriptase and other Type II transmembrane serine proteases inhibitors for treating and preventing viral infections, respiratory disorders, inflammatory disorders, pain disorders, tissue disorders, hyperproliferative disorders, and disorders associated with iron overload. The remaining authors declare that they have no competing interests.

Additional information

Supplementary information The online version contains supplementary material available at https://doi.org/10.1038/s41586-022-04661-w.

Correspondence and requests for materials should be addressed to Richard Leduc, Hector C. Aguilar or François Jean.

Peer review information *Nature* thanks Rolf Hilgenfeld, R Guy and the other, anonymous, reviewer(s) for their contribution to the peer review of this work. Peer review reports are available.

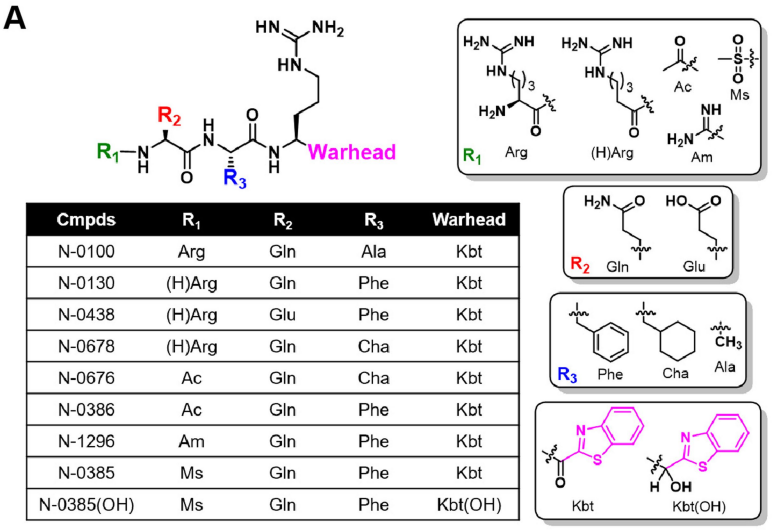

Cmpds	R_1	R_2	R_3	Warhead
N-0100	Arg	Gln	Ala	Kbt
N-0130	(H)Arg	Gln	Phe	Kbt
N-0438	(H)Arg	Glu	Phe	Kbt
N-0678	(H)Arg	Gln	Cha	Kbt
N-0676	Ac	Gln	Cha	Kbt
N-0386	Ac	Gln	Phe	Kbt
N-1296	Am	Gln	Phe	Kbt
N-0385	Ms	Gln	Phe	Kbt
N-0385(OH)	Ms	Gln	Phe	Kbt(OH)

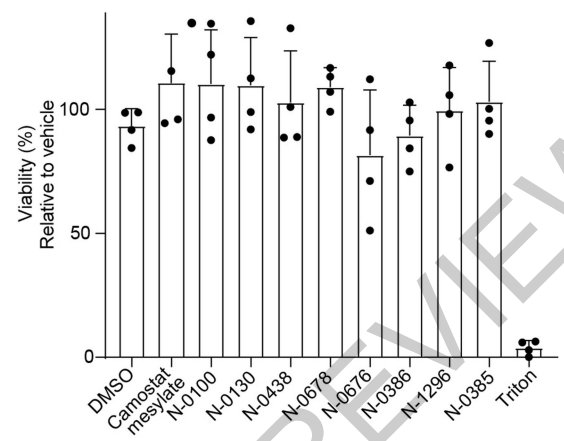

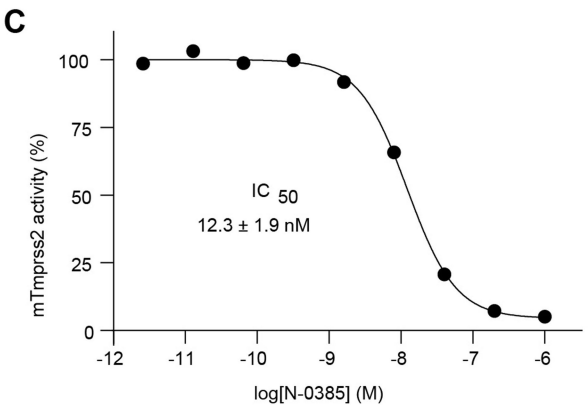

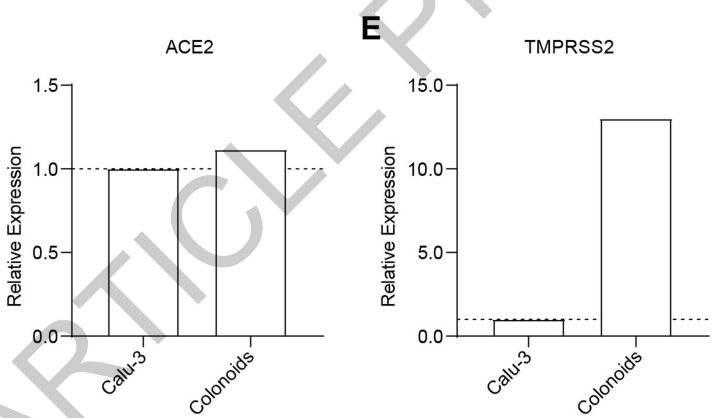

Extended Data Fig. 1 | Peptidomimetic inhibitor characterization. (**A**) Backbone structure of peptidomimetic compounds used in this study along with the groups used in the N-terminal R1 position, R2, R3 and the C-terminal warhead (ketobenzothiazole; kbt) and alcohol warhead (Kbt(OH)). The P1 position is Arginine in all compounds. (**B**) Cytotoxicity of compounds in Vero E6 cells. Cellular viability was evaluated after 24 hr exposure to 10 μM of the indicated compounds (n = 4 independent experiments performed in duplicate). Results are background corrected and presented as the mean viability (%) ± standard deviation (SD) compared to one replicate of vehicle treated cells (DMSO 0.01%) in each experiment. Triton X-100 0.01% was used as a toxicity control. (**C**) N-0385 inhibition of mouse TMPRSS2 (mTMPRSS2). Vero E6 cells were transfected with either an empty vector or mTMPRSS2 for 24 hr. N-0385 was added concomitantly with a fluorogenic substrate on cells for an additional 24 hr before fluorescence reading. Relative activity was measured using the mock-subtracted fluorescence and reported as the percentage of residual activity. Dose-response curves were generated and IC_{50} values were determined using nonlinear regression analysis. One representative IC_{50} curve is shown. The IC_{50} value shown represents the mean ± SD from n = 3 independent experiments. (**D-E**) Real-time PCR analysis for relative expression of (**D**) ACE2 and (**E**) TMPRSS2 expression in Calu-3 cells and colonoids. Relative expression levels normalized using 3 housekeeping genes (YWHAZ, PUM1, MRPL19) are shown for one sample (RNA extract) performed in technical triplicates.

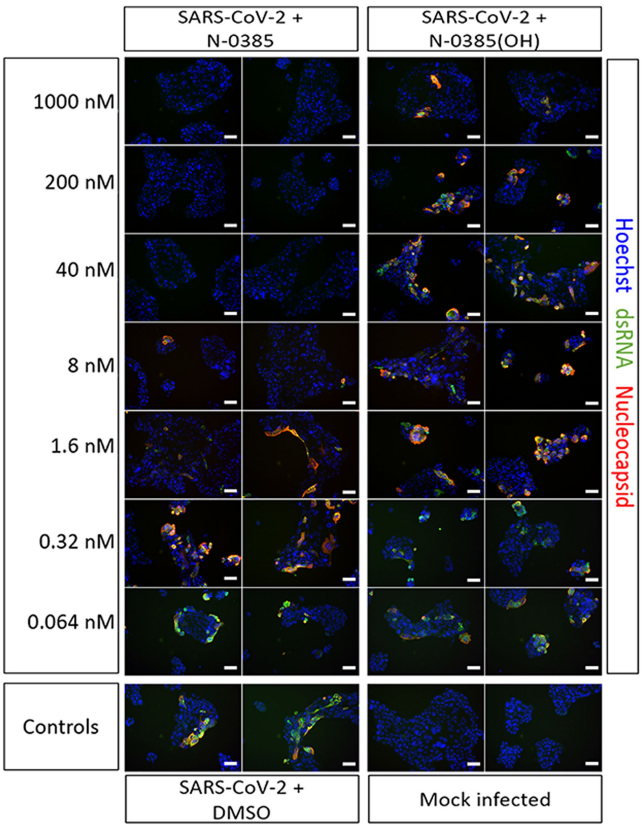

Extended Data Fig. 2 | N-0385 inhibits SARS-CoV-2 infection in a dose dependent manner. Representative images (Cellnsight CX7 High Content Screening platform) are shown from Calu-3 cells treated with the indicated doses of N-0385 and N-0385(OH) for 3 hours prior to infection with SARS-CoV-2 for two days. Cells are stained for Hoechst 33342 (blue), dsRNA (green), nucleocapsid (red). Each image represents one of nine fields of view from a single well of a 96-well plate. Each independent experiment was performed n=8 for N-0385 and n=5 N-0385(OH), with 3 wells of each condition analyzed per experiment. Scale bars = 50 µm.

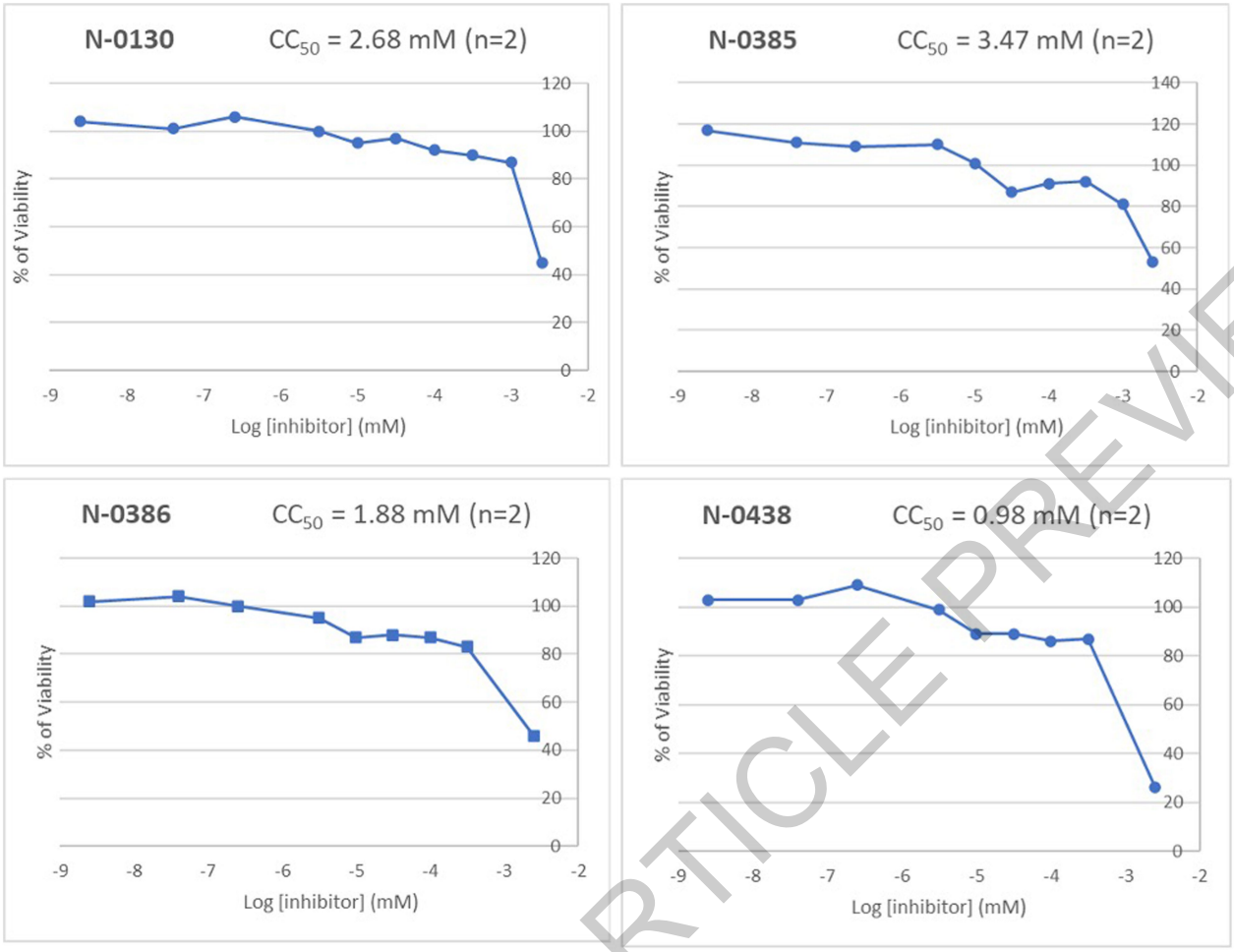

Extended Data Fig. 3 | Dose response CC_{50} (50% cytotoxic concentration) curves for N-130, N-0385, N-0386 and N-0438 in Calu-3 lung epithelial cells. n=2 independent experiments were performed for each compound.

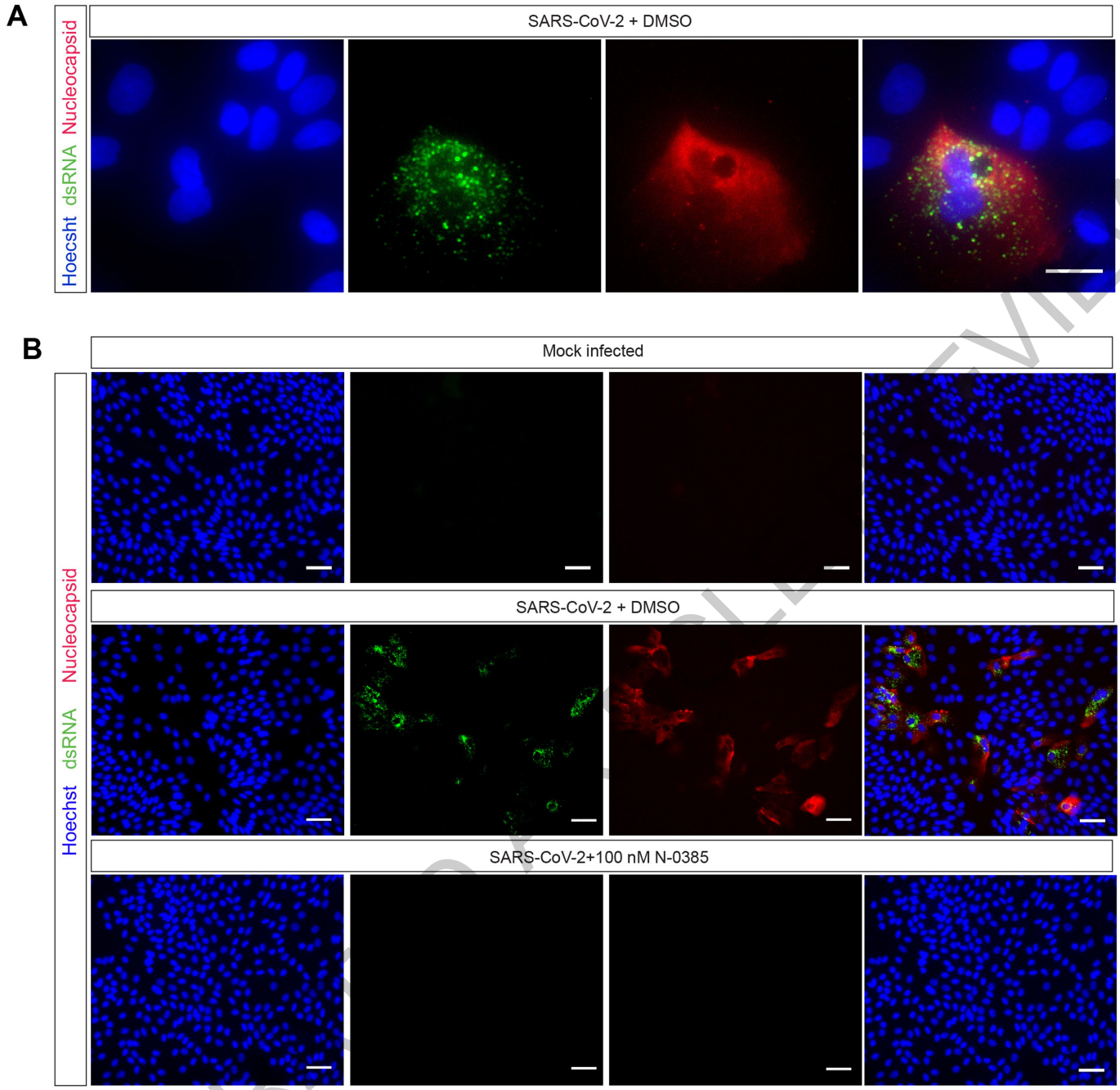

Extended Data Fig. 4 | Representative fluorescent images of SARS-CoV-2 infected colonoids. (**A**) Colonoids infected with SARS-CoV-2 + 0.1% DMSO are shown. Scale bar: 20 µm. (**B**) Mock, SARS-CoV-2 infected, and SARS-CoV-2 + 100 nM N-0385 treated colonoids are shown. Images in (**B**) represent Hoechst, dsRNA, Nucleoscapsid and composite images presented in Fig. 2D. Scale bars are 50 µm. For (**A**) and (**B**) Hoechst is shown in blue, nucleocapsid in red and dsRNA in green. Images captured with EVOS™ M7000 Imaging System. The images are representative of n=3 independent experiments.

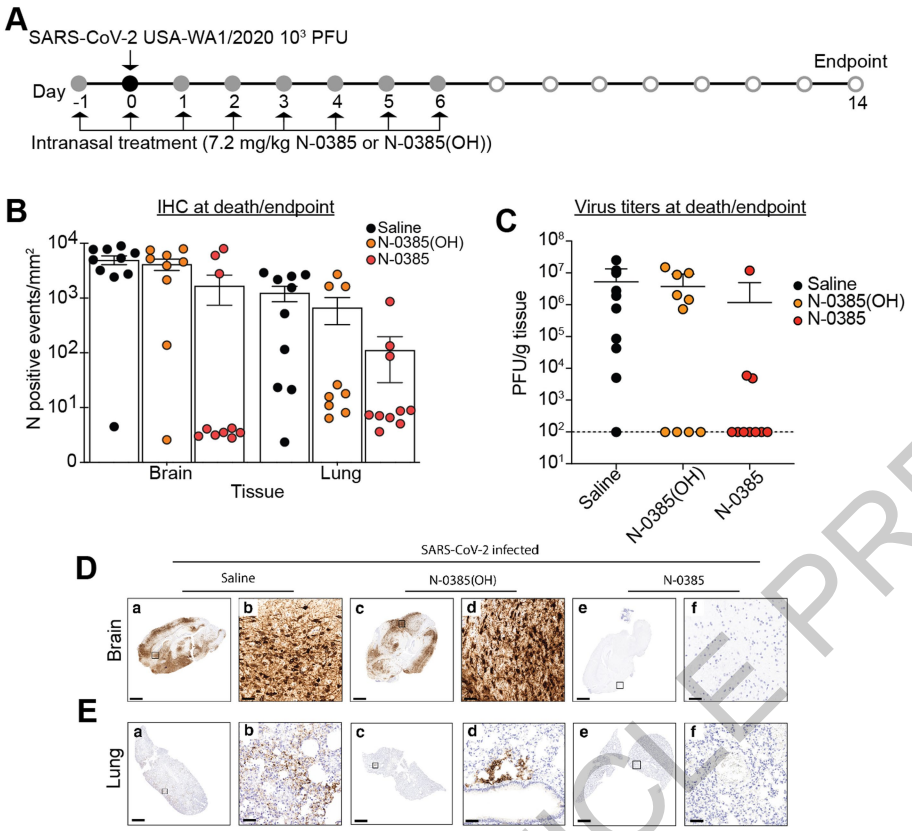

Extended Data Fig. 5 | SARS-CoV-2 in the lungs of mice treated with N-0385 as demonstrated by immunohistochemistry (IHC) and plaque assay. (**A**) Mice were treated daily on days −1 to +6 relative to challenge, with surviving mice terminated on Day 14 (same mice as Fig. 4). (**B**) Number of cells/mm^2 positive for SARS-CoV-2 nucleocapsid (N) at time of death or endpoint by IHC staining. One whole lung slice evaluated per animal. Data presented are mean ± SD (**C**) Virus titers (plaque-forming unit (PFU)/g of tissue) from the lungs of infected mice at time of death or endpoint. Plaque assays were performed twice using a sample from each mouse and the average used to determine PFU/g. Data presented are mean ± SD (**D**) Representative sections of SARS-CoV-2 N staining in the brains of SARS-CoV-2 infected mice at time of death or endpoint. Mice treated with saline (**a, b**: day 8) often had positive immunoreactivity in neurons throughout the brain. Immunoreactivity for SARS-CoV-2 was rare to absent in mice that survived to the study endpoint (**c, d, e, f:** day 14). (**E**) Representative sections of SARS-CoV-2 nucleocapsid in the lung of SARS-CoV-2-infected mice at time of death or endpoint. Mice treated with saline (**a, b:** day 7) had immunoreactivity against SARS-CoV-2 throughout the lung. A similar pattern of patchy infection was present in mice treated with N-0385(OH) (**c, d**: day 6) but was not present in all mice. Immunoreactivity for SARS-CoV-2 was rare to absent in N-0385-treated mice that survived to the study endpoint (**e, f**: day 14). Scale bar for **D, E**: **a, c, e** = 1 mm; **b, d, f** = 50 µm. For each experiment, 10 mice (5 males; 5 females) were analyzed per treatment group. For histopathology and IHC analyses, representative images were selected based on the prevalent trend for a given treatment group, showing images representative of the mean pathological score.

Extended Data Table 1 | Effective dose response values (IC_{50} and EC_{50}), cytotoxicity and selectivity of lead peptidomimetic compounds

Compound	Sequence	TMPRSS2 IC_{50} ± SD (nM)	SARS-CoV-2 Nucleocapsid EC_{50} ± SE (nM)	Calu-3 CC_{50} (nM)	Selectivity Index
Camostat mesylate	$C_{21}H_{26}N_4O_8S$	17.5 ± 18.8	10.6 ± 8.4	ND	ND
N-0130	(H)RQFR-kbt	3.1 ± 1.5	30.1 ± 30.1	$2.7 X10^6$	$8.97 X10^4$
N-0438	(H)REFR-kbt	5.2 ± 5.4	35.7 ± 24.5	$9.8 X10^7$	$2.75 X10^6$
N-0386	Ac-QFR-kbt	3.9 ± 4.4	2.3 ± 1.7	$1.9 X10^6$	$8.26 X10^5$
N-0385	Ms-QFR-kbt	1.9 ± 1.4	2.8 ± 1.4	$3.5 X10^6$	$1.25 X10^6$
N-0385(OH)	Ms-QFR-OH	> 10000	> 1000	ND	ND

ND= not determined

Extended Data Table 2 | *In vitro* K_i values calculated for indicated proteases associated with Fig. 1D

Compound	K_i (nM)					
	Matriptase	Hepsin	DESC1	Thrombin	Furin	Cathepsin L
N-0130	0.13 ± 0.03	0.38 ± 0.19	28 ± 10	8231 ± 1546	> 10000	> 10000
N-0385	2.6 ± 0.4	0.57 ± 0.23	26.6 ± 8.8	9271 ± 647	> 10000	6291 ± 3612
N-0386	0.51 ± 0.09	0.60 ± 0.27	9.1 ± 1.9	> 10000	> 10000	7722 ± 142
N-0438	1.11 ± 0.09	0.52 ± 0.07	31 ± 3	> 10000	> 10000	> 10000
Camostat mesylate	5.6 ± 1.0	4.2 ± 1.6	5.8 ± 3.4	621 ± 46	> 10000	> 10000

Mean values ± SD (n = 3, except Cathepsin L vs N-0385 (n = 4))

Extended Data Table 3 | Summary of histologic findings associated with Fig. 4

Group	No.	Sex	DPI	Alveolar edema	Alveolar fibrin	Perivascular infiltrate in lung	Interstitial infiltrates in lung	Alveolar cells	Type II pneumocyte hyperplasia	Fibrosis	Lymphoid hyperplasia	Perivascular infiltrates in CNS	Necrotic cells in CNS	Gliosis in CNS	Meningeal infiltrate
Saline	1	F	8	1	0	1	3	1	0	0	0	3	5	+	+
	2	F	6	1	1	3	1	1	0	0	0	3	3	+	-
	3	F	6	2	1	2	1	1	0	0	0	2	5	+	-
	4	F	6	0	1	2	1	1	1	0	0	2	0	-	-
	5	F	8	1	4	4	2	4	1	0	0	0	0	-	-
	6	M	7	3	2	3	1	2	1	0	0	1	1	+	+
	7	M	7	0	0	1	0	0	0	0	0	3	4	+	+
	8	M	7	1	1	2	0	0	0	0	0	1	2	+	+
	9	M	7	0	1	2	1	1	0	0	0	3	2	+	+
	10	M	6	1	1	4	2	3	1	0	0	1	0	-	-
N-0385 (OH)	11	F	6	0	0	1	1	0	0	0	0	0	0	-	-
	12	F	7	1	0	3	1	1	1	0	0	2	1	-	-
	13	F	7	0	0	1	0	0	0	0	0	3	3	+	-
	14	F	14	0	0	1	1	0	0	0	0	0	0	-	-
	15	F	14	0	0	1	0	0	0	0	0	1	0	-	-
	16	M	6	0	0	1	0	0	0	0	0	1	0	-	-
	17	M	6	1	1	3	1	1	1	0	0	0	0	-	-
	18	M	1	0	0	0	0	0	0	0	0	0	0	-	-
	19	M	9	2	2	3	3	2	3	0	0	3	2	+	+
	20	M	6	0	0	0	0	0	0	0	0	0	0	-	-
N-0385	21	F	14	0	0	3	2	2	2	2	1	0	0	-	-
	22	F	14	0	0	3	1	1	1	1	1	0	0	-	-
	23	F	14	0	0	1	0	0	0	0	0	0	0	-	-
	24	F	14	0	0	0	0	0	0	0	0	0	0	-	-
	25	F	14	0	0	1	0	0	0	0	0	0	0	-	-
	26	M	14	0	0	3	1	1	3	1	0	0	0	-	-
	27	M	7	0	0	1	1	1	1	0	0	3	4	+	+
	28	M	8	0	0	0	0	0	0	0	0	1	2	+	+
	29	M	8	0	0	1	1	0	0	0	0	3	4	+	+
	30	M	14	0	0	1	1	0	1	0	0	0	0	-	-

For lung, scores were applied based on the percentage of each tissue type (alveolus, vessels, etc.) affected using the following criteria: (0) normal, (1) <10% affected, (2) 10-25% affected, (3) 26-50% affected, and (4) > 50% affected. For brain, histologic scoring was assessed for perivascular inflammation using the most severely affected vessel and the following criteria: (0) no perivascular inflammation, (1) incomplete cuff one cell layer thick, (2) complete cuff one cell layer thick, (3) complete cuff two to three cells thick, and (4) complete cuff four or more cells thick. Necrotic cells in the neuroparenchyma were assessed per 0.237 mm^2 field using the most severely affected area and the following criteria: (0) no necrotic cells (1) rare individual necrotic cells, (2) fewer than 10 necrotic cells, (3) 11 to 25 necrotic cells, (4) 26 to 50 necrotic cells, and (5) greater than 50 cells. DPI = days post-infection.

Extended Data Table 4 | Summary of immunohistochemistry detections using digital image analysis associated with Extended Data Fig. 5D, E

				Brain					Lung				
	No.	DPI	Sex	No. Detections	No. Positive	Positive %	No. Positive per mm^2	Area μm^2	No. Detections	No. Positive	Positive %	No. Positive per mm^2	Area μm^2
Saline	1	8	F	453970	223965	49.33	4974.6	45021429	301943	336	0.2314	23.29	30008571
	2	6	F	486359	374830	77.07	7773	48222090	400667	98447	24.57	2493.4	39483142
	3	6	F	465854	354560	76.11	7696.1	46069957	207789	62226	29.95	2896.7	21481719
	4	6	F	513887	453237	88.2	8910.8	50863741	255267	2896	1.134	115.17	25144846
	5	8	F	386549	171	0.0442	4.474	38217449	178717	27164	15.2	1545	17582272
	6	7	M	537250	128731	23.96	2410.9	53394910	390592	84093	21.53	2174.6	38670869
	7	7	M	408114	215853	52.89	5331.7	40484653	236916	55	0.0232	2.346	23445269
	8	7	M	451316	142848	31.65	3201.4	44620512	215343	456	0.2118	21.32	21389039
	9	7	M	429536	281501	65.54	6610.5	42583630	257917	13211	5.122	518.16	25495909
	10	6	M	355731	97118	27.3	2735.5	35503394	208496	54762	26.27	2657.2	20608928
N-0385(OH)	11	6	F	455410	205622	45.15	4555.9	45133288	147523	39230	26.59	2703.8	14509382
	12	7	F	392653	308647	78.61	7896.3	39087554	385579	61582	15.97	1622.2	37962415
	13	7	F	568631	423604	74.5	7494	56525916	220955	572	0.2589	26.11	21908738
	14	14	F	327808	84	0.0256	2.578	32589614	239373	191	0.0798	8.074	23655852
	15	14	F	370250	143563	38.77	3909.6	36720851	202231	315	0.1558	15.79	19949559
	16	6	M	399074	207074	51.89	5209.1	39752588	290098	315	0.1086	10.94	28784410
	17	6	M	456688	97743	21.4	2144.6	45575843	229152	37366	16.31	1638.9	22799350
	18	1	M	199686	210	0.1052	10.67	19687474	281521	98	0.0348	3.505	27961503
	19	9	M	297118	4043	1.361	137.97	29303917	215259	384	0.1784	17.97	21363623
	20	6	M	521415	310256	59.5	6010.9	51615283	282546	178	0.063	6.38	27900718
N-0385	21	14	F	407628	113	0.0277	2.79	40507501	295210	192	0.065	6.545	29335514
	22	14	F	439501	131	0.0298	3.006	43573511	260794	131	0.0502	5.06	25889492
	23	14	F	585651	205	0.035	3.517	58293602	177531	152	0.0856	8.682	17507867
	24	14	F	611836	255	0.0417	4.198	60744423	186909	131	0.0701	7.096	18461399
	25	14	F	423553	133	0.0314	3.156	42136757	259815	95	0.0366	3.624	26215486
	26	14	M	497724	201	0.0404	4.077	49300400	370766	269	0.0726	7.345	36623344
	27	7	M	539950	429346	79.52	7967.3	53888613	231935	3067	1.322	133.68	22943342
	28	8	M	497665	137295	27.59	2771	49546591	193088	1648	0.8535	86.7	19007209
	29	8	M	459106	271623	59.16	5985.4	45380625	335357	28511	8.502	861.5	33094589
	30	14	M	360472	125	0.0347	3.495	35767364	308928	272	0.088	8.911	30522750

Extended Data Table 5 | Summary of histologic findings in the lung associated with Fig. 6G

Group	No.	Sex	DPI	Perivascular infiltrate in lung	Interstitial infiltrates in lung	Alveolar cells	Type II pneumocyte hyperplasia	Total Score
N-0385	1	F	3	1	1	0	0	2
	2	F	3	1	1	0	0	2
	3	F	3	1	1	0	1	3
	4	F	3	0	1	0	0	1
	5	F	3	0	1	0	0	1
	6	M	3	3	2	1	1	7
	7	M	3	0	1	0	0	1
	8	M	3	1	1	0	0	2
	9	M	3	1	1	0	0	2
	10	M	3	2	2	0	2	6
Saline	21	F	3	2	2	1	2	7
	22	F	3	1	1	0	1	3
	23	F	3	3	2	1	2	8
	24	F	3	1	0	0	0	1
	25	F	3	1	1	0	1	3
	26	M	3	2	2	1	2	7
	27	M	3	3	3	1	3	10
	28	M	3	1	1	1	1	4
	29	M	3	1	0	0	0	1
	30	M	3	2	2	2	2	8

Scores were applied based on the percentage of each tissue type (alveolus etc.) affected using the following criteria: (0) normal, (1) <10% affected, (2) 10-25% affected, (3) 26-50% affected, and (4) > 50% affected. Assessment was performed on tissue sections stained for immunohistochemistry analysis.

nature research

Corresponding author(s): Dr. François Jean, Dr. Richard Leduc, Dr. Hector C. Aguilar

Last updated by author(s): January 18, 2022

Reporting Summary

Nature Research wishes to improve the reproducibility of the work that we publish. This form provides structure for consistency and transparency in reporting. For further information on Nature Research policies, see our Editorial Policies and the Editorial Policy Checklist.

Statistics

For all statistical analyses, confirm that the following items are present in the figure legend, table legend, main text, or Methods section.

n/a	Confirmed	
☐	☒	The exact sample size (*n*) for each experimental group/condition, given as a discrete number and unit of measurement
☐	☒	A statement on whether measurements were taken from distinct samples or whether the same sample was measured repeatedly
☐	☒	The statistical test(s) used AND whether they are one- or two-sided *Only common tests should be described solely by name; describe more complex techniques in the Methods section.*
☒	☐	A description of all covariates tested
☐	☒	A description of any assumptions or corrections, such as tests of normality and adjustment for multiple comparisons
☐	☒	A full description of the statistical parameters including central tendency (e.g. means) or other basic estimates (e.g. regression coefficient) AND variation (e.g. standard deviation) or associated estimates of uncertainty (e.g. confidence intervals)
☐	☒	For null hypothesis testing, the test statistic (e.g. *F*, *t*, *r*) with confidence intervals, effect sizes, degrees of freedom and *P* value noted *Give P values as exact values whenever suitable.*
☒	☐	For Bayesian analysis, information on the choice of priors and Markov chain Monte Carlo settings
☒	☐	For hierarchical and complex designs, identification of the appropriate level for tests and full reporting of outcomes
☒	☐	Estimates of effect sizes (e.g. Cohen's *d*, Pearson's *r*), indicating how they were calculated

Our web collection on statistics for biologists contains articles on many of the points above.

Software and code

Policy information about availability of computer code

Data collection	No software was used to collect data in this study
Data analysis	Molecular Operating Environment (MOE2019.01.02) from the Chemical Computing Group used to generate the TMPRSS2 model with N-0385; (HCS Studio Cell Analysis Software, version 4.0) was used to quantify viral markers of SARS-CoV-2 infection; The GraphPad Prism 9™ (GraphPad Software, Inc.) was used for statistical analysis; Digital image analysis for mouse/nucleocapsid staining was performed using QuPath software version 0.2.3; Leica Application Suite X (LAS X) software was used for acquiring confocal images. Merging of different channels from confocal imaging and the addition of the scale bar were performed using ImageJ/FIJI.

For manuscripts utilizing custom algorithms or software that are central to the research but not yet described in published literature, software must be made available to editors and reviewers. We strongly encourage code deposition in a community repository (e.g. GitHub). See the Nature Research guidelines for submitting code & software for further information.

Data

Policy information about availability of data

All manuscripts must include a data availability statement. This statement should provide the following information, where applicable:

- Accession codes, unique identifiers, or web links for publicly available datasets
- A list of figures that have associated raw data
- A description of any restrictions on data availability

All data generated or analyzed during this study are included in this published article (and its supplementary information files).

Field-specific reporting

Please select the one below that is the best fit for your research. If you are not sure, read the appropriate sections before making your selection.

☒ Life sciences ☐ Behavioural & social sciences ☐ Ecological, evolutionary & environmental sciences

For a reference copy of the document with all sections, see nature.com/documents/nr-reporting-summary-flat.pdf

Life sciences study design

All studies must disclose on these points even when the disclosure is negative.

Sample size	Ten mice were used per group based on the following power analysis statistical power calculations: We sought a sample size that was large enough to detect significant differences in the EC50 averages (+/- standard deviations) between groups. We sought help from the Cornell Statistical Consulting Unit to perform our power analysis. For this, we used our pilot data and a 2-group, 2 sided analysis, setting our power (1-) to 0.9, to have 90% power to detect a statistical difference, and an error rate of 5%, to achieve a significance level of corresponding to a 5% error. These calculations resulted in an N number of animals per groups of seven. However, 10 animals were used to ensure statistical significance in the case of unexpected animal deaths. No sample size calculations were performed for in vitro and cell culture experiments. Sample sizes were based on standards in the field, typically 3 independent biological experiments with each replicate assayed in technical triplicate or greater. Peptidomimetic screening (Fig 2a) against SARS-CoV-2 in Calu-3 was performed only twice (two independent experiments with 5 technical replicates each) to identify the lead compound for detailed downstream analysis. Real-time qPCR was only performed once to qualitatively verify the expression of ACE2 and TMPRSS2 in Calu-3 and colonoids. Due to limited sample availability, the control compound N-0385(OH) was only evaluated against SARS-CoV-2 twice in colonoids and the results were consistent in both experiments. Note that the active compounds N-0385 was tested independently three times in colonoids against SARS-CoV-2.
Data exclusions	1 male animal was excluded from the N-0385(OH) control group that died of unknown causes (day -1-6 treatment), that did not affect statistical significance when excluded or included. GraphPad Prism was used to identify and eliminate outliers (Q = 1) for inhibitor screening, IC50 determination and protease selectivity (Ki).
Replication	Each experiment using 10 mice per treatment group (5 female and 5 male) was performed once. The number of animals used is sufficient to interpret the results with an error rate <5% using male and female animals precluding the necessity of conducting animal experiments in replicate. Also, each animal is considered an independent biological replicate.
Randomization	Mice were designated into groups randomly to reduce bias due to differences in weight, and animal studies were performed using age matched mice to compare across groups. Randomization does not apply to cell-based and in vitro experiments, in which large numbers of cells or reagent aliquots from a given source are partitioned among experimental conditions.
Blinding	Investigators were not blinded to groups during weighing and scoring of animal health due to nature of the infectious agent but histopathology, IHC, and related data analyses were dealt with in a blinded fashion by certified pathologist and clinicians in the team. Blinding was also not done for in vitro or cell-based experiments as no subjective rating of data was involved. Quantification was automated using plate readers, qPCR machines, high-content screening platforms.

Reporting for specific materials, systems and methods

We require information from authors about some types of materials, experimental systems and methods used in many studies. Here, indicate whether each material, system or method listed is relevant to your study. If you are not sure if a list item applies to your research, read the appropriate section before selecting a response.

Materials & experimental systems

n/a	Involved in the study
☐	☒ Antibodies
☐	☒ Eukaryotic cell lines
☒	☐ Palaeontology and archaeology
☐	☒ Animals and other organisms
☒	☐ Human research participants
☒	☐ Clinical data
☐	☒ Dual use research of concern

Methods

n/a	Involved in the study
☒	☐ ChIP-seq
☒	☐ Flow cytometry
☒	☐ MRI-based neuroimaging

Antibodies

Antibodies used	The SARS-CoV-2 nucleocapsid antibody [HL344] (GTX635679) was provided by Genetex; mouse anti-dsRNA antibody (J2-1904) was purchased from Scicons English and Scientific Consulting; Hoechst 33258 and secondary antibodies goat anti-mouse IgG Alexa Fluor 488 (A11001) and goat anti-rabbit IgG Alexa Fluor 555 (A21428) were obtained from Invitrogen
Validation	The nucleocapsid antibody was validated by the company (Genetex) using validation protocols in line with guidelines described by the International Working Group on Antibody Validation (IWGAV). Detailed validation and testing are available here: https://www.genetex.com/Product/Detail/SARS-CoV-2-COVID-19-nucleocapsid-antibody-HL344/GTX635679#datasheet. The manufacturer also states that "This antibody detects SARS-CoV-2 nucleocapsid protein, but does not cross-react with SARS-CoV or MERS-CoV nucleocapsid proteins based on our internal testing." The dsRNA antibody was validated by SCICONS: https://www.jenabioscience.com/rna-technologies/rna-analysis-detection/dsrna-detection/rnt-sci-10010-anti-dsrna-monoclonal-antibody-j2. The manufacturer states: "Specificity: Anti-dsRNA monoclonal antibody J2 recognises double-stranded RNA (dsRNA) provided that the length of the helix is greater than or equal to 40 bp. dsRNA-recognition is independent of the sequence and nucleotide composition of the antigen. All naturally occurring dsRNAs investigated up to now (40-50 species) as well as poly(I)-poly(C) and poly(A)-poly(U) have been recognised by Anti-dsRNA monoclonal antibody J2 although in some assays its affinity to poly(I)-poly(C) is about 10 times lower than that to other dsRNA antigens." Secondary antibodies and Hoecsht were validated by Invitrogen / Thermo Fisher Both nucleocapsid and dsRNA antibodies were additionally verified for specificity using SARS-CoV-2 infected versus non-infected cells as shown in Extended Data Figure 2 and 4 (see mock vs. SARS-CoV-2 panels) where the antibody signal is not detected in non-infected / mock cells.

Eukaryotic cell lines

Policy information about cell lines

Cell line source(s)	All cell lines (Calu-3 cells (ATCC® HTB-55™) and Vero E6 cells (ATCC® CRL-1586™)) were purchased from ATCC (American Type Culture Collection)
Authentication	None of the cell lines used were authenticated
Mycoplasma contamination	We confirm that all cell lines used tested negative for mycoplasma contamination
Commonly misidentified lines (See ICLAC register)	No commonly misidentified cell lines were used in this study

Animals and other organisms

Policy information about studies involving animals; ARRIVE guidelines recommended for reporting animal research

Laboratory animals	Eight-week-old heterozygous K18 hACE2 c57BL/6J male and female mice (strain: 2B6.Cg-Tg(K18-hACE2)2Prlmn/J) were obtained directly from or bred at Cornell using Jackson Laboratory obtained animals. The rodent housing setting includes a standard 12:12 dark/light cycle (for non-breeding rooms), with a temperature range of 68-72 F (20 to 22 °C), and a relative humidity in the range of 40-60%.
Wild animals	The study did not involve wild animals
Field-collected samples	No field collected samples were used in this study
Ethics oversight	Studies were approved and supervised following protocols set and reviewed under Institutional Animal Care and Use Committee at Cornell University (IACUC mouse protocol # 2017-0108 and BSL3 IBC # MUA-16371-1)

Note that full information on the approval of the study protocol must also be provided in the manuscript.

Dual use research of concern

Policy information about dual use research of concern

Hazards

Could the accidental, deliberate or reckless misuse of agents or technologies generated in the work, or the application of information presented in the manuscript, pose a threat to:

No	Yes	
☐	☒	Public health
☐	☒	National security
☒	☐	Crops and/or livestock
☒	☐	Ecosystems
☒	☐	Any other significant area

Hazards: Use of SARS-CoV-2 and SARS-CoV-2 variants of concern (risk group 3 agent)

For examples of agents subject to oversight, see the United States Government Policy for Institutional Oversight of Life Sciences Dual Use Research of Concern.

Experiments of concern

Does the work involve any of these experiments of concern:

No	Yes	
☒	☐	Demonstrate how to render a vaccine ineffective
☒	☐	Confer resistance to therapeutically useful antibiotics or antiviral agents
☒	☐	Enhance the virulence of a pathogen or render a nonpathogen virulent
☒	☐	Increase transmissibility of a pathogen
☒	☐	Alter the host range of a pathogen
☒	☐	Enable evasion of diagnostic/detection modalities
☒	☐	Enable the weaponization of a biological agent or toxin
☒	☐	Any other potentially harmful combination of experiments and agents

Precautions and benefits

Biosecurity precautions	All infections were carried out in a Biosafety Level 3 (BSL3) facility (UBC FINDER) in accordance with the Public Health Agency of Canada and UBC FINDER regulations (UBC BSL3 Permit # B20-0105 to FJ). Animal studies were performed under approved BSL-3 conditions and approved by the Institutional Animal Care and Use Committee at Cornell University (IACUC mouse protocol # 2017-0108 and BSL3 IBC # MUA-16371-1). All animal experiments were performed under USA CDC and USDA guidelines.
Biosecurity oversight	FINDER is UBC's shared platform for researchers working with Risk Group 3 pathogens. Bio-security oversight is provided by The FINDER Steering Committee members and the UBC Vice-President, Research and Innovation Group. All animal BSL-3 work at Cornell University is reviewed by both the IACUC and IBC committees.
Benefits	Benefit is that this work may mitigate risks to public health by providing new antiviral treatment options for SARS-CoV-2 associated disease (COVID-19)
Communication benefits	There are no risks to communicating this information